PIM-1/holey GO mixed matrix membranes for gas separation: unveiling the role of holes

Jose Miguel Luque-Alled [a], Marzieh Tamaddondar [b], Andrew B. Foster [b], Peter M. Budd [b], Patricia Gorgojo [a,c,d]∗

[a] Department of Chemical Engineering and Analytical Science, School of Engineering, The University of Manchester, Oxford Road, Manchester, M13 9PL, United Kingdom

[b] Department of Chemistry, School of Natural Sciences, The University of Manchester, Oxford Road, Manchester, M13 9PL, United Kingdom

[c] Nanoscience and Materials Institute of Aragón (INMA) CSIC-Universidad de Zaragoza, C/ Mariano Esquillor s/n, 50018 Zaragoza, Spain

[d] Chemical and Environmental Engineering Department, Universidad de Zaragoza, C/ Pedro Cerbuna 12, 50009 Zaragoza, Spain

∗ Corresponding author:

p.gorgojo@manchester.ac.uk (P. Gorgojo)

1

Abstract

PIM-1/holey graphene oxide (GO) mixed matrix membranes (MMMs) have been prepared and their gas separation performance for CO_2/CH_4 mixtures assessed. Nanopores have been created in the basal plane of gas-impermeable GO by chemical etching reactions, and the resulting holey flakes have been further chemically functionalized, either with octadecylamine (ODA) or with PIM-1 moieties, to aid their dispersion in PIM-1. It is found that nanopores barely promote gas transport through the graphene-like nanofiller for fresh membranes (tested right after preparation); however, the prepared hybrid PIM-1/holey GO membranes exhibit higher CO_2 permeability and CO_2/CH_4 selectivity than the pure polymer membrane 150 days after preparation; 13 and 15% higher CO_2 permeability for filler contents of 0.1% of octadecylamine-functionalized holey GO and 1% of (PIM-1)-functionalized holey GO, respectively. The most significant improvement is observed for the mitigation of physical aging, as MMMs using 10% of (PIM-1)-functionalized holey GO nanofillers are capable of maintaining up to 70% of their initial CO_2 permeability after 150 days, whereas only 53% is kept for pure PIM-1 after the same period. The gas permeability of the nanofiller has been rationalized with the aid of the Maxwell-Wagner-Sillars equation.

Keywords

1. Introduction

Natural gas and biogas are considered as cleaner alternatives to coal and oil for heat and energy generation.[1] However, in order to cut greenhouse emissions, reduce the volume of gas transport and prevent pipeline corrosion, the final CO_2 concentration of the fuel gas must be reduced to 2-3 mol%.[1, 2] In addition, high concentrations of CO_2 significantly reduce the calorific value of the fuel, leading to revenue losses. The conventionally used technique for CO_2 separations is based on amine absorption processes, which are inherently energy intensive and come with large capital costs derived from the large equipment size that is required.[3] Membrane technology is an alternative to amine absorption capable of producing the desired quality products at lower price and with lower energy usage. The majority of the capital costs of the membrane systems are related to membrane fabrication, membrane modules and pressure systems (compressors and pumps).[4] Due to the highly energy-efficient nature of the process, membrane systems also have low operational costs.[1] Since membranes can be tailored to satisfy different requirements, membrane-based separations are highly flexible and applicable for diverse conditions and environments.[5] Therefore, despite amine absorption remaining as the state-of-the-art technology, membranes are of particular interest for application in remote locations where simple and small-scale units are preferred.[4] Commercial membranes for CO_2 removal from natural gas consist of polymer films packed in large-scale membrane modules. Among these polymeric materials, cellulose acetate membranes hold approximately 80% of the market of membranes used in natural gas treatment.[4] The attractive features of this polymer include the inexpensive and renewable nature of the polymer source and its acceptable performance for CO_2-based separations.[6] Polyimide membranes attracted substantial attention due to their higher CO_2 permeability and

3

CO_2/CH_4 selectivity at laboratory scale, as compared to cellulose acetate membranes. However, the performance of polyimide membranes becomes very similar to that of cellulose acetate when operated at industrial conditions (i.e. 10-60 bar, 30-50 °C and presence of residual contaminants such as heavy hydrocarbons) due to higher sensitivity to plasticization than cellulose acetate and damage to the membrane by the presence of impurities.[7]

Very often, cellulose acetate and polyimide membranes exhibit insufficient CO_2 separation performance, which makes the membrane process economically unfavorable compared to conventionally used amine absorption units.[8] The discovery of new polymers capable of achieving higher gas permeabilities and satisfactory CO_2/CH_4 selectivities has therefore dominated the research at laboratory scale during the last few decades. Among these novel structures, a new family of polymers known as polymers of intrinsic microporosity, PIMs, have gathered lots of attention.[9] Their rigid and contorted backbones result in inefficient packing of the polymer chains and creates large voids and high free volume which are responsible for the high gas permeabilities of PIMs.[10] In addition, these large voids are connected by narrow cavities that leading to an acceptable CO_2/CH_4 membrane selectivity. The best studied member of this family for gas separation applications in general, and for CO_2 separation from natural gas in particular, is known as PIM-1.[11] Many years of research have demonstrated its potential to play a significant role in the development of future membranes.[12, 13] However, it has also been shown that the performance of PIM-1 membranes drastically worsens over time; after a PIM-1 film is formed the polymer chains slowly rearrange, losing most of the polymer excess free volume and thus reducing the gas permeabilitiy. This effect is known as "physical aging" and is common to all glassy high free volume polymers.[14] In addition, polymer free volume loss is accelerated when thin membranes are used (selective layers around 100-

4

200 nm thick are typically required for industrial applications). Hence, physical aging is the main limitation for their use in industrial separations.[14] Apart from gas separation membranes, PIMs and PIMs-based composite materials have also a strong potential for a large number of applications, among many others water treatment,[15] energy storage,[16] redox flow batteries,[16] fuel cells,[16] H_2 storage,[17] breathable materials[18] and sensors.[19] More specifically, PIM-1/graphene materials have been reported for membrane pervaporation,[20, 21] hydrogels for environmental remediation[22] and substrates/promoters for catalysis and for sensing.[23]

A common strategy to enhance the gas separation performance of PIM-1 membranes is the use of fillers, and the formation of what is known as mixed-matrix membranes (MMMs). Several types of fillers, including metal organic frameworks (MOFs),[24] polymer nanosheets,[25] and graphene-based materials,[26-28] have been incorporated in PIM-1 matrices, boosting the performance of the membranes. However, only a few studies reported fillers capable of improving the initial membrane performance along with mitigation of physical aging; e. g. porous aromatic framework PAF-1,[29] polyhedral oligomeric silsesquioxane (POSS),[30] PIM-1 nanosheets,[25] (PIM-1)-functionalized UiO-66-NH$_2$,[24] and (PIM-1)-functionalized beta-cyclodextrin.[31]

The addition of graphene-based nanofillers into PIM-1 as a strategy to prevent physical aging has been studied at The University of Manchester. We have reported the use of alkyl-functionalized GO and reduced GO,[27] organosilane-functionalized graphene oxide (APTS-GO) and (PIM-1)-functionalized GO.[28] Graphene-based nanofillers hold a clear advantage over other type of fillers, such as PAFs[29] and MOFs,[24] as their ultrathin 2D nature allows the preparation of thin film membranes of a few hundreds of nanometers containing graphene-like nanofillers.[21, 32] Nonetheless, so far results have shown that the addition of graphene-based nanofillers leads to a large decrease in the initial CO_2 and CH_4

permeabilities, which is more pronounced as the loading increases.[27, 28] This has been attributed to the non-porous nature of the nanofiller, and the subsequent increase in tortuosity of the gas molecule pathways and lower diffusion coefficient as compared to the base polymer.[33] Alternatively, the incorporation of nano-pores in graphene oxide (GO) has been proven to increase the diffusivity of MMMs made with other polymers than PIM-1, with pores acting as "open gates" for the transport of gases through the polymer sieve.[34]

In this manuscript, we report the use of holey GO nanofillers in PIM-1 membranes to minimize the large decrease in gas permeability seen with the addition of non-holey graphene-like fillers we have previously reported,[27, 28] while maintaining the reduction in physical aging over time. In order to achieve a good dispersion in the polymer matrix, GO has been functionalized with octadecylamine or PIM-1 chains. The prepared MMMs have been tested up to 150 days to study the evolution of physical aging and the role of the graphene-like nanofillers on the final gas permeability.

2. Experimental section

2.1. Materials

3,3,3',3'-tetramethyl-1,1'-spirobisindane-5,5',6',6'-tetrol (TTSBI) and potassium permanganate ($KMnO_4$) were acquired from Alfa Aesar (UK). Sulphuric acid (H_2SO_4), hydrogen peroxide (H_2O_2), anhydrous potassium carbonate (K_2CO_3) and chloroform were provided by Fisher Chemicals (UK). 2,3,5,6-tetrafluoroterephthalonitrile (TFTPN), sodium nitrate ($NaNO_3$), anhydrous dimethylacetamide (DMAc), anhydrous dichlorobenzene (DCB), methanol, ethanol and acetone were purchased from Sigma Aldrich (UK). Graphite was purchased from NGS Naturegraphit GmbH (Germany). Deionized water (DI) employed in this manuscript was obtained using a Milli-Q integral

system (Merck Millipore, Ireland). All chemicals were used as received without further purification.

2.2. Synthesis of PIM-1

PIM-1 was prepared via fast polycondensation as reported elsewhere.[20, 35] 3.4 g (0.01 mol) of TTSBI, 2 g (0.01 mol) of TFTPN, 4.2 g of K_2CO_3 (0.03 mol), were mixed with 20 ml of DMAc and 10 ml of DCB, and reacted under an atmosphere of N_2 with mechanical stirring at 160 °C for 40 min. The reaction was stopped by pouring the mixture into methanol. The polymer was then filtered and thoroughly washed with methanol. To purify the polymer, the solid was dissolved in chloroform, reprecipitated in 400 ml of methanol and collected by vacuum filtration. To remove any K_2CO_3, the polymer was refluxed in water and then collected again by vacuum filtration. Later on, the solid was washed three times with acetone (200 mL for each wash) and three times with methanol (200 mL for each wash), and then left to dry in a vacuum oven at 110 °C for 2 days.

2.3. Synthesis of graphene oxide (GO) and holey GO

GO was synthesized using a modified Hummer's method reported elsewhere.[36] In-plane porosity at nano-scale was created on the GO via treatment with an oxidizing agent as described by Xu et al.[37] 95 ml of an aqueous GO solution (1 mg mL^{-1}) was mixed with 5 mL of H_2O_2 (30 wt %) in a round bottom flask and left under stirring at 100 °C for 4 h. The product (denoted as *HGO-4h*) was filtered using commercial PVDF filters (pore size ~0.1 μm), washed with abundant water and left to dried under N_2 flow. In order to track the oxidation process, another holey GO sample was prepared increasing the reaction time up to 8 h and maintaining the temperature at 100 °C. This sample was denoted as *HGO-*

8h. With the aim of proving the role of H_2O_2 in the oxidation process, a control sample (*cGO*) was obtained by treating GO at 100 °C for 4 h without the addition of H_2O_2.

2.4. Octadecylamine (ODA) functionalization of holey GO

For octadecylamine (ODA) functionalization, a similar procedure to the one reported by Alberto et al. was followed.[20] 100 mg of HGO-4 was dispersed in 95 mL of DI water and transferred to a round bottom flask. 0.27 g of ODA was dissolved in 5 mL of ethanol and then, added to the holey GO dispersion. The mixture was heated up to 60 °C for 12 h. Afterwards, the resulting powder named ODA-HGO-4h was purified by filtration over a filter paper and washed with ethanol (200 ml, twice) and chloroform (200 ml, three times). The sample was dried under vacuum at room temperature for 12 h.

2.5. (PIM-1)-functionalization of holey GO

In order to covalently bind PIM-1 to the graphene nanosheets, TTSBI and TFTPN monomers were reacted in the presence of HGO-4h according to the following procedure: 0.34 g (0.001 mol) of TTSBI, 0.2 g (0.001 mol) of TFTPN, 0.42 g (0.003 mol) of K_2CO_3 and 56 mg of HGO-4h were mixed with 30 mL of DMF and reacted under continuous N_2 flow at 70 °C for 24 h. In order to quench the reaction, the mixture was poured into a beaker with 200 mL of methanol. Afterwards, the collected solid was then redispersed in chloroform and reprecipitated by addition of excess methanol. Later, the mixture was filtered to remove the mixture of solvents, placed in water and heated overnight under reflux conditions. The dispersion was then filtered, washed with methanol (100 ml, three times) and acetone (100 ml, three times), and left to dry under vacuum at 80 °C. The obtained greenish powder was denoted as *P-H24*, where "P" stands for PIM-1, "H" refers to HGO-4h and "24" corresponds to the reaction time. P-H24 is expected to contain

unattached PIM-1 along with PIM-1 covalently bound to HGO-4h, as reported in our previous work for GO.[28] Therefore, P-H24 underwent a further purification procedure (a series of dissolutions in chloroform and filtration steps described in our previous publication[28]) with the aim of removing the unattached PIM-1 and isolating what is believed to be purely PIM-1 covalently bound to HGO-4h. This material is denoted as *f-P-H24* where "f" stands for "filtered".

2.6. Materials characterization

The molecular weight of PIM-1 was determined using a multi-detector Viscotek GPCmax VE 2001 gel chromatograph (Malvern, UK) equipped with two PLgel mixed-B columns and Viscotek TDA302 triple detector array. For the analysis, a solution of 1 mg ml^{-1} of PIM-1 in chloroform was filtered through a PTFE filter with a pore size of 0.34 μm and injected into the column using a flow rate of 1 mL min^{-1}. For the analysis of the data, OMNISEC software (Malvern, UK) was used.

Proton nuclear magnetic resonance spectroscopy (1H NMR) data were acquired with a Bruker Advance II 500 MHz instrument (Bruker, UK) using a PIM-1 solution in deuterated chloroform with a concentration of 0.01 g mL^{-1}.

Elemental analysis of PIM-1, HGO-4h and P-H24 was investigated using a Flash 2000 Organic Elemental Analyzer (Thermo Scientific, The Netherlands).

A Micromeritics ASAP 2020 volumetric adsorption analyzer (Micromeritics, USA) was employed to obtain the adsorption and desorption N_2 isotherms of PIM-1 and P-H24, and their surface area was calculated from the sorption isotherms using the Brunauer–Emmett–Teller (BET) method.

X-ray photoelectron spectroscopy (XPS) measurements were conducted using an Axis Ultra spectrometer (Kratos Analytical Limited, Manchester, UK) equipped with a

monochromatic Al Kα source (1486.7 eV). In order to investigate the chemistry of all the synthesized materials, the high resolution XPS spectra of C1s, O1s and N1s were obtained and analyzed with CasaXPS software.

Attenuated total reflectance Fourier transform infrared spectroscopy (ATR-FTIR) measurements were obtained using an Alpha-P FTIR spectrometer (Bruker, UK) and a Germanium crystal as background.

Thermogravimetric analysis (TGA) was performed using a SDT 650 Thermal Analyzer (TA Instruments, USA) under a N_2 atmosphere, within a temperature range from 25 to 800 °C and using a heating rate of 10 °C min^{-1}.

UV-Vis absorption measurements were performed using a Shimadzu UV-2700 spectrophotometer (Shimadzu, Japan) and quartz cuvettes.

GO, cGO, HGO-4h and HGO-8h were also characterized by Raman and methylene blue (MB) adsorption experiments. Raman spectroscopy measurements were conducted using a WITec Apyron Raman spectroscope with a laser excitation wavelength of 532 nm. MB adsorption experiments were done following a similar procedure to that described elsewhere[37, 38] and explained in detail in the supporting information (section 2.2. Methylene blue adsorption experiments of GO, cGO, HGO-4h and HGO-8h).

Transmission electron microscopy (TEM) using a FEI Tecnai G2 20 microscope (FEI, USA) equipped with an X-Max EDX detector operating at 200 kV was employed to investigate the morphology of all the graphene-like materials. TEM specimens were prepared by drop casting of the graphene dispersion on a lacey carbon film on 200 mesh copper grids (Agar Scientific).

2.7. Membrane fabrication

MMMs were prepared by a blending method where the nanofillers (either ODA-HGO-4h or P-H24) were first dispersed in chloroform at a concentration of 1 mg ml^{-1} by means of sonication for 2 h. The graphene dispersion was then mixed with a PIM-1 solution in chloroform so as to have a final concentration of polymer of 5 wt %. The solution was then stirred for 2 h and probe sonicated for 10 min (power of 60 W on a discontinuous mode consisting of 10 s of sonication pulses at intervals of 3 s). The solutions were transferred immediately after sonication to glass petri-dishes, placed inside a cabinet under continuous flow of N$_2$ and each petri-dish was covered with a lid to slow down the evaporation rate. After two days, the solvent had evaporated and the membranes were peeled off from the petri dish, soaked in methanol for 24 h and dried in a vacuum oven for 12 h at 10 mbar and 80 °C. Pure PIM-1 membranes were also prepared. Table 1 sums up the specifications of all membranes tested in this manuscript. It should be noted that the name of the nanofiller was given to the resultant MMMs.

Table 1. Details of all MMMs tested for CO_2/CH_4 separations in this study including name, filler specification and filler loadings.

Membrane name	Filler loadings (wt %)	Filler specification
PIM-1	-	No filler
ODA-HGO-4h	0.1, 0.2 and 0.5	100 wt % ODA-HGO-4h
P-H24	1, 5 and 10	~9.4 wt % (PIM-1)-functionalized HGO-4h * + ~90.6 wt % unattached PIM-1 *

* Values of (PIM-1)-functionalized HGO-4h and unattached PIM-1 presented in this table correspond to those obtained by UV-Vis analysis.

2.8.   Membrane characterization

The membrane thickness was measured using a digital micrometer screw gauge (Mitutoyo IP65 Coolant Proof, UK) with an accuracy of $\pm\,0.5$ µm. Values are the average of at least five different measurements at different locations across the tested membrane sample and are given with their corresponding standard deviation.

Cross-section and top-view scanning electron microscopy (SEM) images were acquired obtained using a FEI Quanta 650 FEG-SEM microscope (FEI, USA). Cross-section specimens were prepared by fracture of small pieces of membrane that had been previously immersed in ethanol for a few seconds and then in liquid N_2 for 10 s. The step of soaking the membrane in ethanol allows for a clean fracture due to sorption of ethanol in the polymer free volume that freezes the film more effectively. To render electrical conductivity to the polymeric SEM specimens, all samples were coated with platinum using a MTM 10 Thickness Monitor (Cressington, USA) sputter coating system prior to imaging.

2.9.   Gas separation measurements

Pure PIM-1 membranes and MMMs were evaluated for CO_2/CH_4 separations at a constant temperature of 25 °C. As a feed gas, a binary mixture of CO_2 and CH_4 (50:50) with a flow rate of 25 ml min^{-1} was used, and a pressure difference of roughly 1.5 bar between the feed and permeate side was set. Gases were analyzed with a microchromatograph (Agilent 490 microGC) equipped with a PoraPlotU column and a

thermal conductivity detector. A schematic illustration of the gas separation rig described above is available in our previous article.[27]

The long-term performance of the membranes was studied over 150 days, with the membranes tested every 30 days (i.e. at 0, 30, 60, 90, 120 and 150 days after membrane preparation), with the exception of MMMs containing P-H24 that were not tested at 120 days. All membranes were kept in a parafilm-sealed box stored in a dark and dry place when they were not being tested. The gas permeability was calculated from Eq. 1 in Barrer units (1 Barrer = 10^{-10} cm^3 (STP) cm cm^{-2} s^{-1} cmHg^{-1}).

$$P = \frac{Q \, l}{A \, \Delta p} \tag{1}$$

where Q (cm^3 (STP) s^{-1}) corresponds to the gas flow rate in the permeate, l (cm) is the thickness of the membrane, A (cm^2) is the effective area of the membrane, and Δp (cmHg) corresponds to the gas partial pressure difference across the membrane.

The real CO_2/CH_4 selectivity of the membranes was calculated as the ratio of gas permeabilities using Eq. 2:

$$CO_2/CH_4 \text{ selectivity} = \frac{P_{CO_2}}{P_{CH_4}} \tag{2}$$

Two main parameters were used to assess the degree of physical aging in the membranes: i) the CO_2 permeability drop and ii) the relative CO_2 permeability, which were calculated at different times of aging t_1 (given in days) using Eq. 3 and Eq. 4, respectively.

$$CO_2 \text{ permeability drop at } t_1 = \text{Initial } P_{CO_2} - P_{CO_2} \text{ at } t_1 \tag{3}$$

$$\text{Relative } P_{CO_2} \text{ at } t_1 = \frac{P_{CO_2} \text{ at } t_1}{\text{Initial } P_{CO_2}} \tag{4}$$

3. Results and discussion

3.1. Characterization of GO, Holey GO (HGO-4h) and ODA-functionalized holey GO (ODA-HGO-4h)

Several materials were synthesized with the aim of studying the formation of nano-holes in GO by chemical etching using H_2O_2 as oxidizing agent. XPS was employed to investigate the chemistry of GO, the materials resulting from its oxidation (HGO-4h and HGO-8h), GO reacted without the addition of the oxidizing agent (cGO) and HGO-4 functionalized with ODA. C1s high resolution XPS spectra of GO, cGO, HGO-4h, HGO-8h and ODA-HGO-4h are presented in Figure 1. The spectrum of the control sample cGO is very similar to that of GO, which confirms that without the addition of H_2O_2 the oxidation process does not take place.[37] This also proves that at the temperature of 100 °C the reduction of GO by water molecules does not occur to a significant extent, which would be observed as a noticeable decrease in the intensity of the C-O and C=O peaks.[39] However, both HGO-4h and HGO-8h show a significant decrease in the peak corresponding to C-O and a small increase in that associated with C=O groups, as expected. In addition, these features are more prominent for HGO-8h as compared to HGO-4h, due to the longer reaction time and higher degree of oxidation. Oxidation process of GO with H_2O_2 leads to ketone, lactone and carboxyl group formation (i.e. conversion of C-O into C=O) which, promoted by the elevated temperature, results in scission of oxygen functional groups, forming CO and CO_2,

and thus creating vacancies (i.e. nano-holes) in the 2D nanosheet.[40] Figure S1 shows a schematic representation of the formation of nanopores in HGO-4h, where the removal of carbon atoms neighboring the oxygen functional groups involved in the oxidation reactions can be observed. A high resolution XPS spectrum of C1s (Figure 1e) was also acquired for ODA-HGO-4h (octadecylamine-functionalized HGO-4h prepared to allow stable dispersions of the holey graphene-like material in chloroform) and compared with that of non-functionalized HGO-4h. After ODA functionalization, the peak associated with C-O is substantially smaller and a new peak corresponding to C-N is observed. Moreover, there is also a positional shift in the peak attributed to carbonyl groups, from 288.8 eV to 287.9 eV, as a consequence of nucleophilic substitution and amide formation.[41] The chemical structure suggested for ODA-HGO-4h is illustrated in Figure S2.

The high resolution XPS spectra of O1s and N1s for all the materials can be found in the supporting information (Figure S3). The content of each element as atomic % was calculated from the ratio of the areas contained in each high resolution spectrum. Additionally, the degree of functionalization in ODA-HGO-4h was calculated as explained in the supporting information using the atomic % shown in Table S1. The analysis showed that ODA-HGO-4h consists approximately of 56 wt % of octadecyl chains and 44 wt % of HGO-4h.
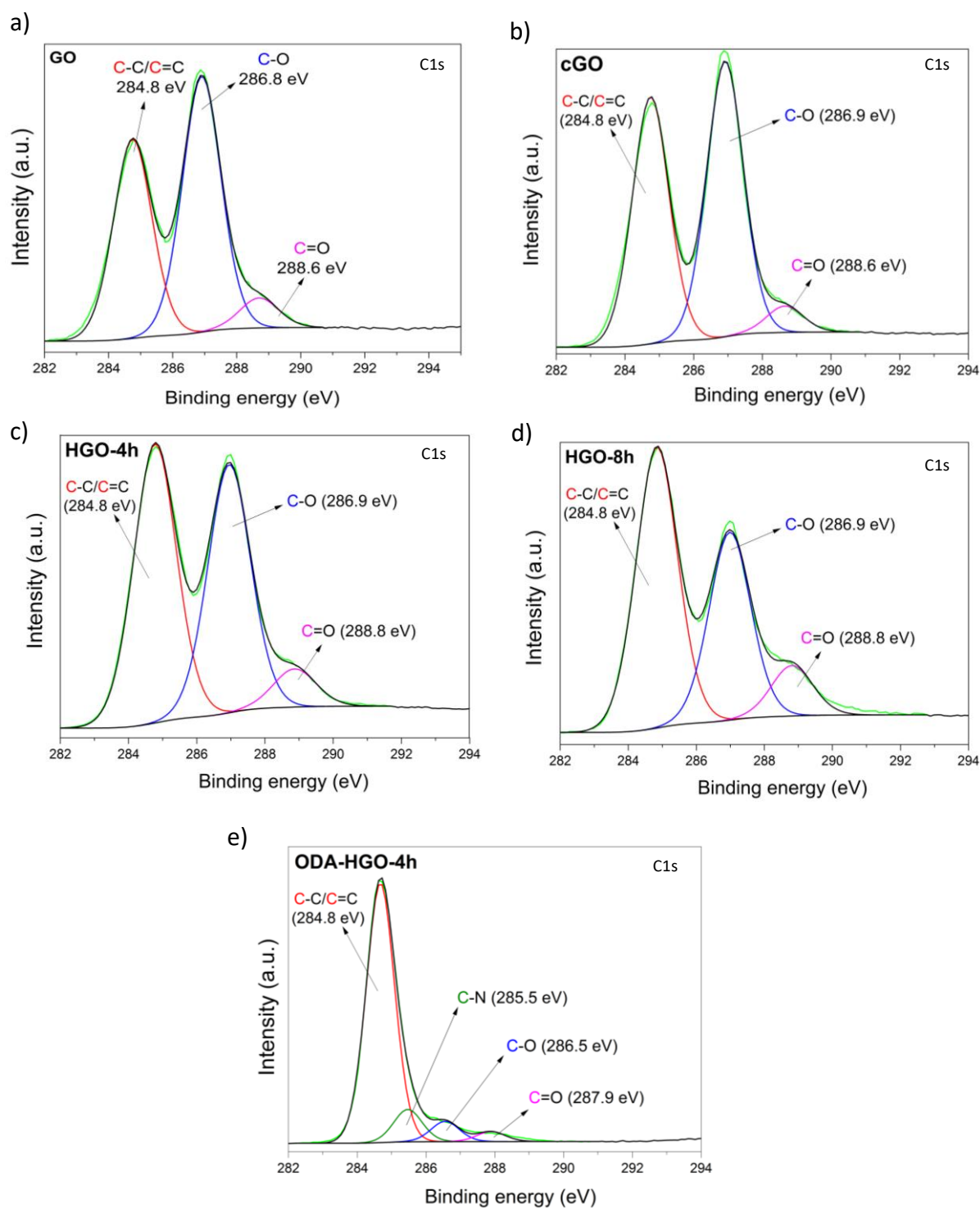
Figure 1. C1s high resolution XPS spectra of GO (a), cGO (b), HGO-4h (c), HGO-8h (d) and ODA-HGO-4h (e). In all the XPS spectra, the green line represents the acquired XPS signal, whereas the black line corresponds to the fitted spectrum which includes the contributions of all the individual peaks.

MB adsorption tests were conducted to investigate the available surface area of GO, cGO, HGO-4h and HGO-8h in aqueous dispersions. This method has been proven to be more reliable than N_2 adsorption experiments where agglomeration of the graphene layers in dried samples leads to low surface area values.[37, 42, 43] It is hypothesized that the introduction of pores in the basal plane of the graphene layer increases the porosity and therefore the adsorption capacity towards MB dyes. This was confirmed by the values obtained in this work, which are in good agreement with other values reported in the literature.[37, 42, 43] HGO-8h shows the highest surface area (1395 m^2 g^{-1}) followed by HGO-4h (1203 m^2 g^{-1}), whereas GO and cGO exhibit similar surface area (1059 and 908 m^2 g^{-1}, respectively). MB calibration curves and average UV-Vis absorption spectra of the supernatant for all the experiment using GO, cGO, HGO-4h and HGO-8h are presented in the supporting information (Figure S4).

FTIR spectroscopy analysis of GO, HGO-4h and ODA-HGO-4h is available in the supporting information (Figure S5). FTIR of HGO-4h shows an increase in the intensity of the bands associated with C=O and a decrease in intensity of those bands belonging to OH vibrations, as compared to that of GO, which agrees with the results from the XPS analysis and suggests that oxidation reactions occur in the GO structure. The FTIR spectrum of ODA-HGO-4h confirms the covalent grafting of the alkyl chain, as evidenced by the appearance of characteristic bands from C-N, N-C=O and CH_2 vibrations (Figure S5). Characterization by Raman spectroscopy of GO and HGO-4h also suggests the removal of oxygen-containing functional groups and consequently formation of nano-holes in the 2D structure. A more detailed explanation is found along with the Raman spectra in the supporting information (Figure S6).

TEM images for GO, cGO, HGO-4h and HGO-8h were acquired to study the pore formation process, the influence of the reaction time and the effect of the oxidizing agent.

Both GO (Figure 2a) and cGO (Figure 2b) display homogeneous surfaces with absence of pores. HGO-4h (Figure 2c and 2.d) shows numerous irregularities and several nanometric pores within the range of 1.5 and 5 nm, similar in size to those reported by other authors.[37, 44] More images of cGO and HGO-4h can be found in the supporting information (Figure S7a-d). As observed in HGO-8h (Figure S7e and S7f), the number and size of the pores increased with the reaction time.[37, 44] However, a broken structure with very wide distribution of pores ranging from approximately 10 to 200 nm is revealed. As aforementioned, the pore formation process occurs in the regions containing oxygen functional groups, where nanopores are produced as a consequence of CO and CO_2 formation.[37, 40, 44] The created nanopores typically contain several oxygen functional groups at the edges, so that if prolonged reaction times are allowed further oxidation takes place and bigger pores are formed.[37, 44] Moreover, according to the most accepted structure of GO[45], discrete "islands" containing epoxide, hydroxyl, ketone and carboxylic groups are separated by graphitic regions. Therefore, functional groups in the discrete "islands" are close to each other, which means that pore growth will eventually result in the merging of two small pores to form a much bigger one. Thus, longer reaction times mainly lead to much larger pores instead of creation of new nanopores.
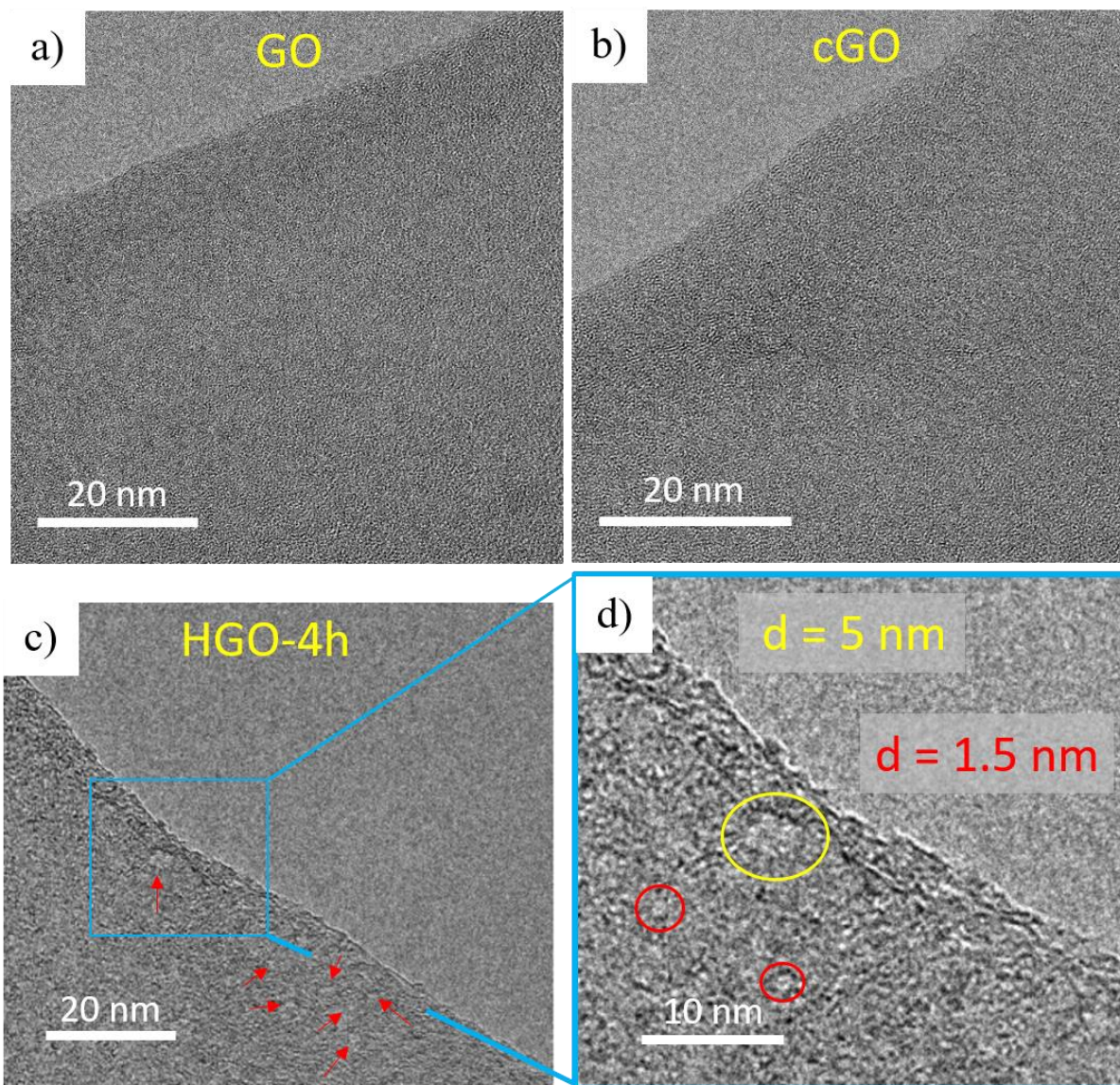
Figure 2. TEM images of GO (a) and cGO (b) at high magnification, and HGO-4h (c and d) at high magnification.

3.2.   Characterization of PIM-1 and (PIM-1)-functionalized HGO-4h (P-H24)

The synthesized PIM-1 was characterized prior to the preparation of the MMMs. The GPC analysis gave a weight-average molar mass (M_w) of 165 kg mol^{-1} with a dispersity of 2.3, and the BET surface area obtained from the N$_2$ adsorption-desorption analysis was 794 m^2 g^{-1}. These values confirmed the formation of a highly porous polymer structure

that could be cast into mechanically stable membranes. 1H NMR analysis revealed four characteristic signals corresponding to PIM-1 (Figure S8).

HGO-4 was functionalized with PIM-1 to prevent agglomeration of the GO-like nanofiller in chloroform (solvent used to dissolve PIM-1 prior to membrane formation) and the resulting material was denoted P-H24. In addition, as explained in the experimental section, P-H24 was further purified by undergoing several filtration steps with the aim of removing unattached PIM-1 and the material was denoted f-P-H24. In order to confirm the synthesis of PIM-1 onto HGO-4h (sample P-H24) and the covalent attachment of PIM-1 to HGO-4h, several characterization techniques, including elemental analysis, spectroscopy (FTIR, UV-Vis, XPS), thermogravimetric analysis and TEM, were utilized.

Elemental analysis was performed on P-H24 and compared with that of pure PIM-1 and HGO-4h. As shown in Table S2 in the supporting information, approximately 88.4 wt % of P-H24 corresponds to PIM-1, whereas HGO-4h accounts for the remaining 11.6 wt %. N_2 adsorption and desorption isotherms of P-H24 show very similar sorption properties to PIM-1 (Figure S9), including gas adsorption at the very low-pressure range associated with microporosity, and a calculated BET surface area of 803 m^2 g^{-1}.

Pure PIM-1, P-H24 and f-P-H24 were analyzed via FTIR, and their corresponding spectra are shown in the supporting information (Figure S10). Pure PIM-1 and P-H24 infrared spectra show identical vibration bands, which further confirms the formation of PIM-1 and also suggests the vast majority of sample P-H24 is PIM-1. However, the filtered sample (f-P-H24) does show features corresponding to both PIM-1 and HGO-4. This suggest that the purification process removes the vast majority of PIM-1 (unattached to GO) and leads to a solid which consists of GO covalently bound to PIM-1.

XPS measurements were acquired for f-P-H24 and compared with that of PIM-1 and HGO-4 to investigate the chemical reactions between the graphene nanosheets and the polymer chains. The C1s high resolution XPS spectrum of f-P-H24 (Figure 3b) is quite similar to that of PIM-1 (Figure 3a), showing two peaks corresponding to C-C (accounting for both single and double carbon-carbon bonds) and C-O in both spectra.[15, 46] However, the area ratio of C-C/C-O bonds is higher for f-P-H24 (C-C/C-O area ratio of 2.52) as compared to PIM-1 (C-C/C-O area ratio of 1.99), which indicates that chemical reactions take place between the PIM-1 monomers and the functional groups in HGO-4h. Nucleophilic substitutions between the hydroxyl and alkoxide groups in HGO-4h and the fluorine groups in the TFTPN monomers are expected to occur.[28] These chemical reactions lower the content of C-O bonds in HGO-4h, as inferred from the C1s high resolution XPS spectrum of f-P-H24 with an intensity decrease of the C-O peak (i.e. higher C-C/C-O area ratio) as compared to both PIM-1 and HGO-4h. The peak corresponding to C=O, is seen in both HGO-4h (Figure 1c) and f-P-H24 spectra.
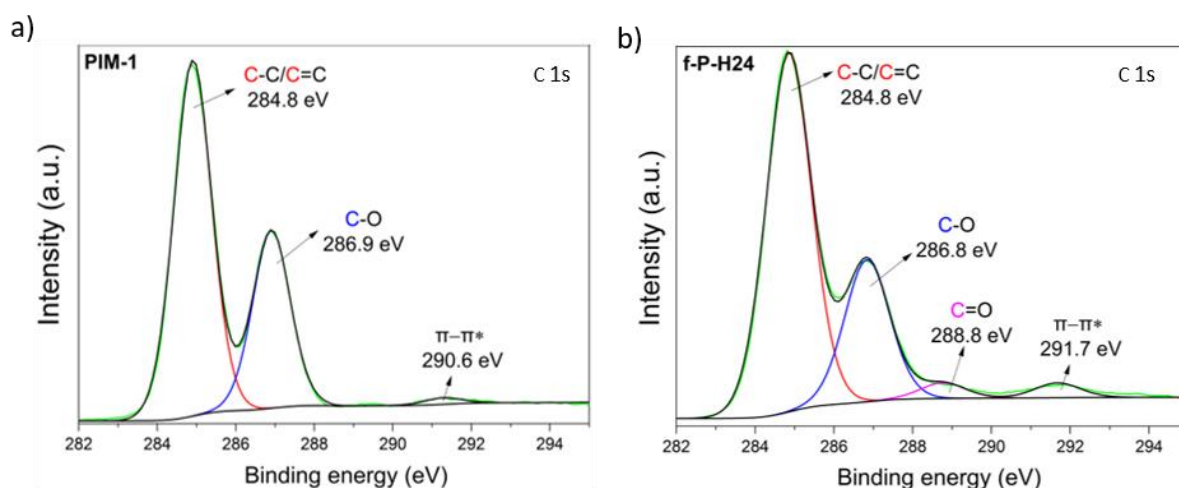

Figure 3. C1s high resolution XPS spectra of PIM-1 (a) and f-P-H24 (b). In all the XPS spectra, the green line represents the acquired XPS signal, whereas the black line corresponds to the fitted spectrum which includes the contributions of all the individual peaks.

The high resolution spectra of O1s (Figure S11) and N1s (Figure S12) are presented and discussed in the supporting information. Atomic % was calculated as the ratio of the areas of the high resolution XPS spectra of C1s, N1s and O1s. The content of PIM-1 in f-P-H24 was estimated using the atomic % of each element following the procedure described in the supporting information. The calculated content of PIM-1 in f-P-H24 is 57.3 wt %.

Thermogravimetric (TGA) measurements (curves shown in Figure S13) also confirm a much higher content of PIM-1 in P-H24 (96 wt %, as compared to 40 wt % in f-P-H24).

UV-Vis spectroscopy of f-P-H24 and HGO-4h (Figure S14) show strong scattering effects from the HGO-4h material, i.e. a continuous increase in the absorbance as the wavelength decreases. The scattering process from the nanomaterial shifts the position of the absorption bands from PIM-1 moieties in f-P-H24 and decreases their absorption intensity.[23] In order to work out the amount of PIM-1 in P-H24 and f-P-H24, a calibration process was followed and then the average UV-Vis absorption values of P-H24 and f-P-H24 were interpolated in the calibration curve. All the calibration curves as well as the UV-Vis absorbance curves of P-H24 and f-P-H24 can be found in the supporting information (Figure S15). UV-Vis measurements suggest a PIM-1 content of 3.3 wt % in f-P-H24, which is much lower than that obtained using XPS (57.3 wt %) and TGA (40 wt %). However, it has been proven that the strong scattering effect of the graphene-like material greatly decreases the absorption intensity of the polymer at low PIM-1 concentrations, giving rise to greatly underestimated PIM-1 content values.[23, 28] Regarding P-H24, UV-Vis measurements indicate a PIM-1 content of 90.6 wt % in the sample, which is similar to the values calculated using TGA (96 wt %) and elemental analysis (88.4 wt %). Discrepancies between the values obtained by different techniques (UV-Vis, TGA and elemental analysis) are believed to be mainly related to water and

solvent adsorbed in PIM-1 and to the presence of polymer chains having different topologies.[47]

TEM images of PIM-1 and f-P-H24 (Figure S16) show amorphous organic matter on top of the graphene flake in the f-P-H24 image, which confirms that PIM-1 has been deposited on the surface of the graphene nanosheet.

3.3. SEM characterization of the membranes

The morphology of pure PIM-1 and MMMs containing both ODA-HGO-4h and P-H24 nanofillers were studied by SEM. Top-view images (Figure S17) are very similar for all membranes (including pure PIM-1), where no pinholes or defects are observed within the resolution of the SEM. Cross sectional images of PIM-1 and MMMs show the typical structure of dense membranes suggesting also the absence of pores or pinholes (Figure 4). Wrinkles and polymer veins are observed in the exposed area of the cross-sectional images for some membranes. These features are seen in both pure PIM-1 and MMMs, and can be related to the cleanness of the freeze-fracture step[28] and strong interactions taking place between the polymer matrix and the filler.[48, 49] In order to provide more hints about the origin of the wrinkles and polymer veins, a higher magnification cross-sectional image of membrane 0.5 % ODA-HGO-4h, which shows plenty of these features, is presented in Figure 4d. This image suggests that the polymer membrane has been torn instead of fractured, resulting in remnants of elongated polymer segments. Moreover, no defects or filler agglomeration in the polymer matrix is observed within the resolution of the SEM. The thicknesses of all membranes were found to be within the range of 40 - 50 µm, similar to the average thickness obtained in measurements using the micrometer (Table S5).
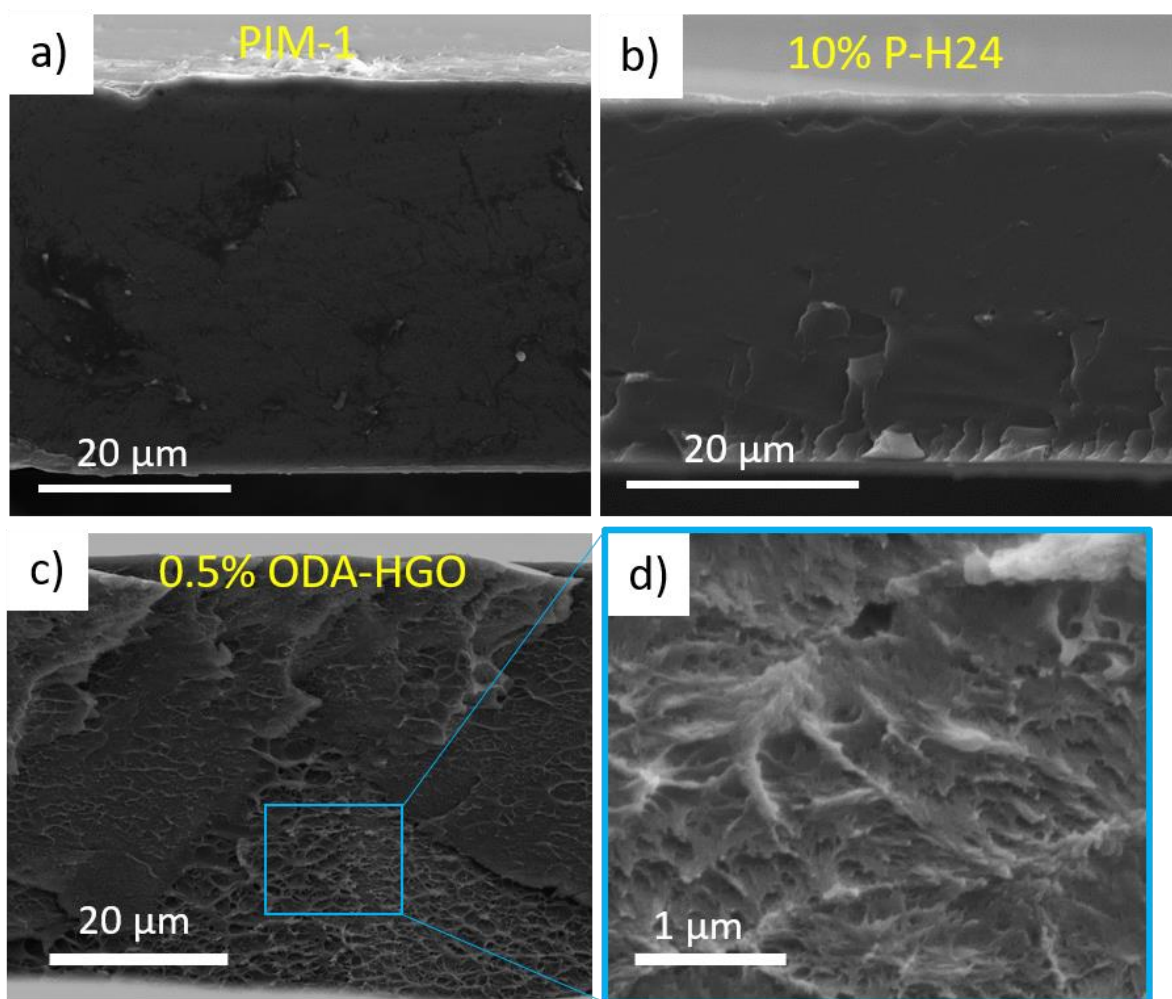
Figure 4. Cross-sectional SEM images for films of PIM-1 (a) and MMMs: 10% P-H24 (b) and 0.5% ODA-HGO-4h (c and d).

3.4. Gas separation performance of MMMs containing holey GO: ODA-HGO-4h and P-H24

Mixed gas separation measurements were undertaken for all the membranes and the CO_2 and CH_4 permeabilities and CO_2/CH_4 selectivity values calculated (Table S6-10). Gas permeability data were obtained from the average of at least four different coupons for each type of membrane; except for PIM-1 that was fabricated and tested as a control membrane along all the MMMs series and consequently, the reported value is the average of twenty-two coupons. This results in a larger standard deviation of gas permeabilities

corresponding to PIM-1 as compared to MMMs (especially after 150 days), however, the large population of permeation data ensures robustness and accuracy of the average value. Post-preparation treatment of soaking the membranes in methanol was conducted as it significantly raises membrane gas permeabilities because of swelling of the polymer chains, releasing polymer free volume and removing solvent molecules trapped within the polymer matrix.[25] The CO_2 permeabilities of MMMs containing ODA-HGO-4h and P-H24 fillers are plotted in Figure 5a and 5b, respectively. It can be seen that different loadings are used depending on the nanofiller. For the preparation of MMMs with ODA-HGO-4h, loadings between 0.1 and 0.5 wt % were selected as higher loadings result in filler agglomeration and very brittle membranes, which leads to irreproducibility of the gas permeation results and usually remarkably high permeabilities and low selectivities. Much higher nanofiller loadings, ranging from 1 to 10 wt %, were used in the preparation of MMMs containing P-H24. As mentioned in section 3.2, P-H24 consists of ~90 wt % unattached PIM-1 and ~10 wt % PIM-1 covalently bound to HGO-4h, so the effective nanofiller loadings are estimated to be roughly 10 times smaller (i.e. effective loadings ranging from 0.1 to 1 wt %). However, these values are still higher than those for ODA-HGO-4h due to a more homogeneous dispersion aided by the PIM-1 functionalization.[24, 28]

The addition of ODA-HGO-4h fillers barely alters the permeation rate of both CO_2 and CH_4 at the lowest filler loading (0.1 wt %), achieving initial CO_2 and CH_4 permeability values of 6,146 (Figure 5a) and 527 (Figure S18a) Barrer, respectively. The addition of higher loadings of ODA-HGO-4h (0.2 and 0.5 wt %) reduces the gas permeabilities for both CO_2 and CH_4, which suggests that even though HGO-4h possesses in-plane porosity, the tortuosity for gas molecules is still higher than in pure PIM-1. This can be attributed to the non-porous fragments in the 2D materials that decreases the diffusion coefficient

(D) of CO_2 and CH_4 in the MMM.[27, 32, 33, 50, 51] In addition, other events may contribute to the lower gas permeabilities: i) pore blockage by octadecyl chains (either by pore functionalization or because octadecyl chains lie on the surface of HGO-4h), and ii) nanofiller agglomeration of even a few layers of ODA-HGO-4h may result in blockage of the in-plane nanopores of the nanosheets. The introduction of ODA-HGO-4h nanofillers reduces the physical aging and results in higher permeability after 150 days as compared to pure PIM-1. This behavior has been previously observed when large particles,[24, 29, 30] including graphene-based nanofillers,[26-28] are incorporated into PIM-1 matrices and is explained by rigidification effects in the polymer chains caused by the presence of the nanofillers. As seen in Figure 5c, there is an optimum loading of ODA-HGO-4h (i.e. 0.2 wt %) that achieves the lowest permeability drop, 1,870 Barrer from the initial value. Values relative to initial CO_2 permeability (Figure S18c) confirm that 0.2 wt % ODA-HGO-4h shows the best performance in terms of preservation of its initial gas permeability, with a relative CO_2 permeability of 0.66. At higher nanofiller loadings of 0.5 wt %, nanomaterial agglomeration is expected, which weakens the ability of the nanofiller to inhibit physical aging.[27] CO_2/CH_4 selectivity values for all MMMs containing ODA-HGO-4h (Figure 5e) remain similar to that of pure PIM-1 (ranging from 11.7 to 15.6 over 150 days of physical aging), with 0.2% ODA-HGO-4h exhibiting the highest CO_2/CH_4 selectivity of 15.7 after 150 days.

MMMs prepared using (PIM-1)-functionalized HGO-4h fillers (P-H24) show a decrease in the CO_2 (Figure 5d) and CH_4 permeabilities (Figure S18c) of fresh membranes, which is higher as the loading of the nanofiller increases; membranes at 10% P-H24 show the lowest average CO_2 permeability (4,727 Barrer). As aforementioned, the decrease in initial gas permeability has been widely reported for MMMs containing GO-like nanofillers and is attributable to a reduction in the gas diffusivity.[27, 32, 33, 50] Similarly

to what happens to other GO-based fillers, the presence of P-H24 also causes rigidification effects (i.e. strong interactions of the nanofillers with the polymer chains) and subsequent partial hindrance of physical aging over time. It is expected that the higher the amount of nanofiller the more available surface area and the lower the physical aging, up to an optimum loading from where undesirable filler agglomeration effects appear. This has been previously discussed for MMMs containing ODA-HGO-4h nanofillers and also seen in other studies.[27, 52] For the prepared MMMs with P-H24, the CO_2 permeability drop follows the sequence 2908 > 1968 > 1576 > 1445 Barrer for PIM-1 (first value) and filler loadings of 1, 5, and 10% (subsequent values). This trend suggests that agglomeration or restacking of GO flakes is nonexistent or minimal. Filler/polymer compatibility is well-known to be an important issue in MMMs and particularly for sheet-like nanofillers due to their extremely high aspect ratios.[51] When using P-H24 nanofillers, the drop in CO_2 permeability over 150 days is lower for the membranes with the highest loading of nanofiller, as seen in Figure 5d (CO_2 permeability drop) and Figure S18d (relative CO_2 permeability). Thus, through chemical functionalization of HGO-4h with PIM-1 moieties, a satisfactory blending with the polymer has been achieved and, very little or no agglomeration of the filler occurs.[28] All MMMs containing P-H24 show slightly higher selectivity values than pure PIM-1 at the initial stages of physical aging (Figure 5f). This has also been observed for other MMMs containing graphene-like nanofillers and has been associated with an enhancement in both diffusivity and solubility selectivities.[33, 50] Upon aging, CO_2/CH_4 selectivities of all membranes increased as observed in Figure 5f.
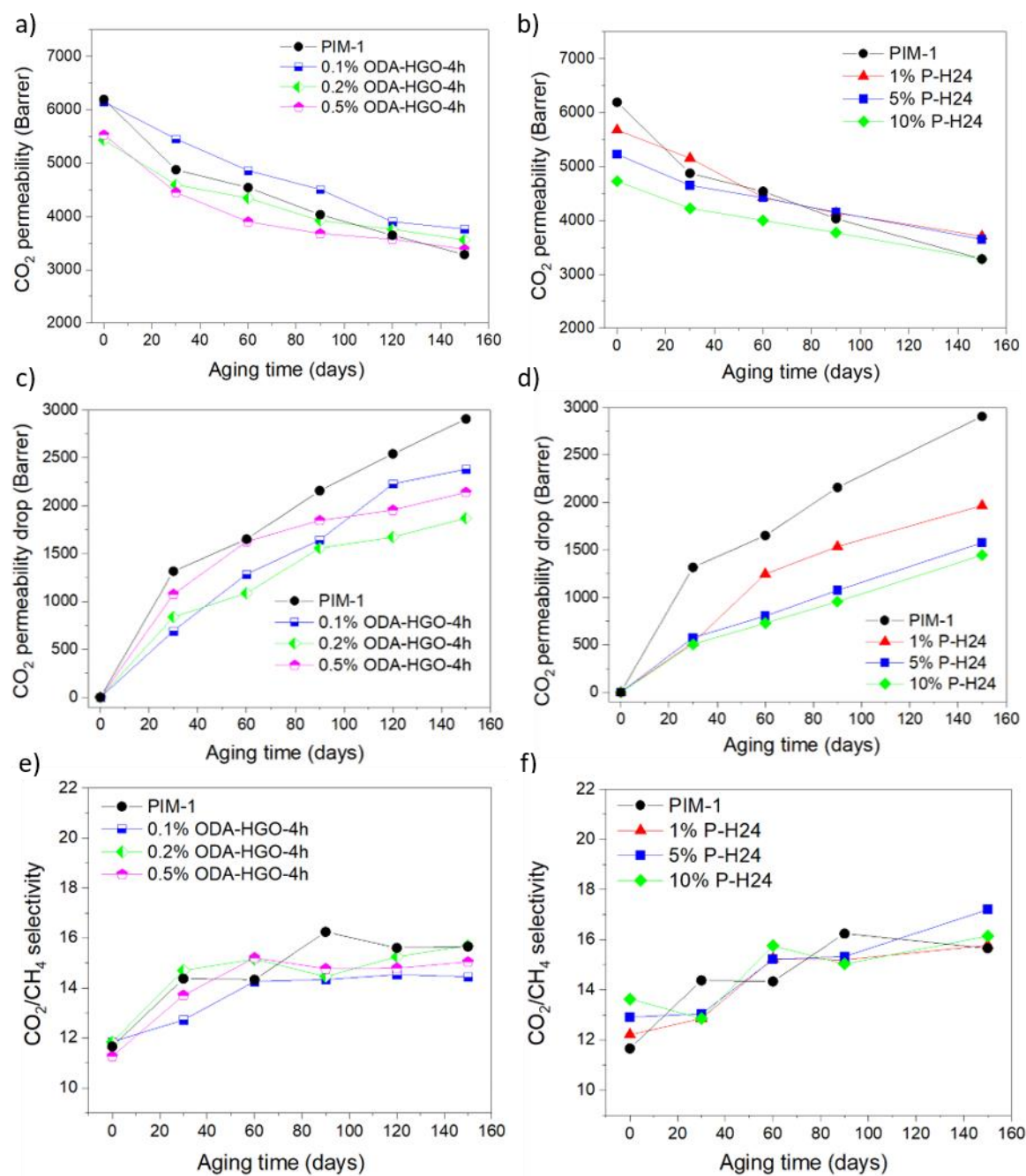
Figure 5. Gas separation performance of PIM-1 and MMMs containing ODA-HGO-4h: CO_2 permeabilities (a), CO_2 permeability drops (c), and CO_2/CH_4 selectivities (e). Gas separation performance of PIM-1 and MMMs containing P-H24: CO_2 permeabilities (b), CO_2 permeability drops (d), and CO_2/CH_4 selectivities (f). Permeability values are the average of at least 4 tested coupons and the standard deviations is shown in Table S6.

3.5. Unveiling the role of nanopores in holey GO

Alkylamine-functionalized GO ODA-HGO-4h can be considered the porous homolog of ODA-GO, since the only difference between both nanofillers is the formation of in-plane nanopores in the former. Our group has previously reported the CO_2/CH_4 separation performance of MMMs containing non-porous ODA-GO,[27] which can be compared to that of membranes presented in this work containing ODA-HGO-4h in order to assess the role of the nanopores. At 0 days of physical aging (fresh membranes), MMMs containing ODA-HGO-4h show higher CO_2 permeabilities than those containing their non-porous counterparts ODA-GO (Table 2), suggesting that the pores of ODA-HGO-4h contribute to increase the transport of gas molecules through the membrane; they act as "open gates" and shorten the molecular pathways.

After 150 days (aged membranes), MMMs prepared using ODA-HGO-4h nanofillers also exhibit higher CO_2 and CH_4 permeabilities than MMMs containing ODA-GO (Table 2). However, the pristine PIM-1 membranes in our previous work suffer a larger extent of physical aging than the ones used in this work over the same period (Table 2); it is worth noting that two different PIM-1 batches were used and observed higher gas permeabilities for MMMs containing ODA-HGO-4h may be related to the polymer itself. Foster et al.[47, 53] found that the presence of branched PIM-1 chains (formed during the polymer synthesis as a consequence of incomplete disubstitutions) results in slower physical aging as compared to linear polymeric structures. NMR characterization (Figure S8) suggests the presence of branched polymer structures within the PIM-1 sample employed in this manuscript, which accounts for the slower physical aging as compared to the PIM-1 sample reported in our previous publication.

The CO_2/CH_4 separation performance of MMMs prepared using P-GO24 nanofillers (non-porous counterpart of P-H24) can be found in another publication from our group, [28] and values are also collected in Table 2. Fresh MMMs (0 days of physical aging) containing P-H24 and P-GO24 nanofillers show very similar CO_2 and CH_4 permeabilities, suggesting that the effect of the nano-holes on the gas permeabilities of these membranes is very limited. This result can be explained by the small pore size and low density of pores, as seen in section 3.1. In addition, PIM-1 functionalization of HGO-4h occurs through chemical reactions of PIM-1 precursors with the oxygen functional groups in HGO-4h, which are located at the edge of the nanopores. [37, 40] Chemical reactions on functional groups surrounding the pore have been proven to result in pore shrinkage for several nanomaterials, including nanoporous graphene [40] and MOFs. [54, 55]

After 150 days of aging the average CO_2 permeability of all the MMMs containing P-H24 are slightly higher than those values obtained for aged MMMs prepared using P-GO24 nanofillers (Table 2). Furthermore, MMMs containing P-H24 with loadings of 1, 5 and 10% show drops in CO_2 permeability of 1,968, 1,576 and 1,445 Barrer, respectively, which are lower than those for membranes prepared with non-porous P-GO24 (2,301, 2,026 and 1,693 Barrer, for 1, 5 and 10% loadings, respectively). A similar trend is observed for the relative CO_2 permeability values. In this case, since the same PIM-1 polymer (from the same batch) has been used in both studies, the fact that all MMMs containing P-H24 show higher CO_2 permeabilities than MMMs containing P-GO24 after the same aging period suggests that the presence of the nanopores in P-H24 has a positive effect on the overall gas permeation.

Gas molecules tend to travel through the polymer pathways that are more energetically favorable (typically larger pores), and thus in fresh membranes where the free volume is at its maximum, gas permeation occurs mainly through the polymer free volume elements

rather than narrow nanopores of the holey GO flakes. However, as the polymer ages, the void elements in PIM-1 decrease in size and gas permeation through the polymer matrix is hindered,[29, 56-59] making the nanopores on the graphene flake a more energetically affordable pathway than before. The transport of gas through the nanofiller becoming more relevant as the polymer ages can explain the observed higher permeabilities after 150 days for the MMMs containing porous GO. This hypothesis has been rationalized with the aid of the Maxwell equation in the following section.

Table 2. Summary of gas separation performance of MMMs containing graphene-like nanofillers. CO_2 and CH_4 permeabilities, and CO_2/CH_4 selectivity at 0 days and 150 days of physical aging along with CO_2 permeability drop and relative to initial CO_2 permeability data.

Membrane	CO_2 permeability at 0 days (after 150 days) in Barrer	CH_4 permeability at 0 days (after 150 days) in Barrer	CO_2/CH_4 selectivity at 0 days (after 150 days) in Barrer	CO_2 permeability drop after 150 days in Barrer (relative CO_2 permeability)	Ref
PIM-1	$6{,}190 \pm 812$ $(3{,}283 \pm 870)$	543 ± 104 (219 ± 73)	11.7 ± 1.8 (15.6 ± 2.6)	$2{,}908$ (0.53)	This study
0.1% ODA-HGO-4h	$6{,}146 \pm 831$ $(3{,}763 \pm 354)$	527 ± 105 (263 ± 31)	11.8 ± 1.0 (14.4 ± 1.7)	$2{,}383$ (0.61)	This study
0.2% ODA-HGO-4h	$5{,}429 \pm 649$ $(3{,}559 \pm 815)$	469 ± 89 (226 ± 46)	11.8 ± 2.2 (15.7 ± 1.2)	$1{,}870$ (0.66)	This study
0.1% ODA-GO[a]	$4{,}800 \pm 1000$ $(2{,}000 \pm 100)$	250 ± 400 (80 ± 100)	18.9 ± 1.2 (26.6 ± 2.6)	$2{,}800$ (0.43)	[27]
0.25% ODA-GO[a]	$4{,}500 \pm 1000$ $(1{,}700 \pm 600)$	250 ± 800 (70 ± 300)	18.3 ± 2.1 (26.3 ± 5.3)	$2{,}800$ (0.38)	[27]
1% P-H24	$5{,}675 \pm 427$ $(3{,}707 \pm 432)$	480 ± 102 (240 ± 51)	12.2 ± 1.9 (15.8 ± 1.8)	$1{,}968$ (0.65)	This study

10% P-H24	4,727 ± 449 (3,283 ± 321)	360 ± 91 (232 ± 120)	13.6 ± 2.3 (16.1 ± 4.0)	1,445 (0.70)	This study
1% P-GO24	5,421 ± 439 (3,120 ± 370)	437 ± 70 (187 ± 33)	12.6 ± 1.6 (16.9 ± 1.1)	2,301 (0.58)	[28]
10% P-GO24	4,808 ± 972 (3,115 ± 434)	422 ± 105 (197 ± 33)	11.6 ± 1.2 (15.9 ± 1.2 1)	1,693 (0.68)	[28]

[a] MMMs prepared with a PIM-1 sample having an initial CO_2 permeability of 6,400 Barrer and a CO_2/CH_4 selectivity of 20.3, and a CO_2 permeability of 2,000 Barrer and a CO_2/CH_4 selectivity of 30 after 150 days of physical aging.

3.6. Rationalization of the MMMs gas separation performance using the Maxwell model

The Maxwell equation is introduced in this manuscript to study the influence of the filler permeability on the overall permeation. The original equation elucidated by Maxwell addressed the dielectric properties of diluted discrete particles embedded in a polymer matrix. However, this equation has been widely applied to study the permeability of MMMs at filler loadings below 0.2 of volume ratio. The Maxwell-Wagner-Sillars equation (Eq. 5) is a modified function of the Maxwell equation which includes a parameter related to the shape and orientation of the fillers and is then more appropriate for non-spherical fillers:[8, 60]

$$P_M = P_p \frac{n P_f + (1 - n) P_p + (1 - n)(P_f - P_p)\emptyset}{n P_f + (1 - n) P_p - n(P_f - P_p)\emptyset} \tag{5}$$

where P_M, P_p and P_f account for the gas permeabilities of the MMM, polymer phase and filler, respectively, $\emptyset$ represents the filler volume ratio and n is the shape factor related to the geometry and the orientation of the filler. For the shape factor ($0 \leq n \leq 1$), the upper and lower limits correspond to a parallel (n=0) and a series (n=1) configuration of the two phases in the MMMs.[61]

As shown in the previous section, MMMs containing ODA-HGO-4h show higher CO_2 and CH_4 permeabilities than those prepared with their non-porous counterparts, ODA-GO nanofillers, which is attributed to higher CO_2 and CH_4 permeabilities of ODA-HGO-4h nanofillers. In order to establish a permeability range for these porous 2D fillers Eq. 5 has been used; firstly, the n parameter related to the shape and orientation of the nanofiller was calculated for those MMMs containing non-porous ODA-GO nanofillers (a more detailed procedure is presented in the supporting information in section 2.18). Calculated n values range from 0.993 to 0.996, which indicates that most of the graphene flakes are arranged parallel to each other and perpendicularly orientated to the gas flow. Based on the assumption that both nanofillers ODA-GO and ODA-HGO-4h have the same orientation and shape, i.e. same factor n, the P_f value can be calculated for each MMM using Eq. 5. The obtained P_f values for ODA-HGO-4h are in the range of 63-898 Barrer for CO_2 and 3.3-31.9 Barrer for CH_4, which are much smaller than the gas permeabilities of the bare polymer (6190 and 543 Barrer for CO_2 and CH_4, respectively).

The gas permeabilities of fresh MMMs containing P-H24 and P-GO24 are remarkably similar, and this precludes the P_f calculation of the (PIM-1)-functionalized HGO nanofiller. The Maxwell-Wagner-Sillars equation above-mentioned (Eq. 5) can be re-organized as in   Eq. 6.

$$\frac{P_M}{P_P} = \frac{\left(\frac{P_f}{P_p}\right)(n + \emptyset - n\emptyset) + (1 - n - \emptyset + n\emptyset)}{\left(\frac{P_f}{P_p}\right)(n - n\emptyset) + (1 - n + n\emptyset)} \tag{6}$$

This function stablishes a simple relationship between the permeability of the filler (P_f) and the polymer (P_p). If a large difference exists between both permeabilities, the following assumption can be made:[62]

if $\quad$ $P_f \ll P_p$ $\quad$ then $\quad$ $\dfrac{P_M}{P_P} = \dfrac{(1-n-\emptyset+n\emptyset)}{(1-n+n\emptyset)}$ $\hfill$ (7)

According to Eq. 7, if the nanofiller permeability is much smaller than the polymer permeability, the effect of the filler permeability is negligible and the permeability of the MMMs is mainly affected by the filler loading ($\emptyset$). The $\dfrac{P_f}{P_p}$ ratio at which the filler permeability becomes mathematically meaningless has been reported to be around 0.1. Bouma et al.[62] gave a suitable explanation to this fact: i) if the permeability of the filler is much lower than that of the polymer, the preferred pathways for the gas molecules are through the polymer matrix going around the filler, ii) then, a further reduction in the filler permeability will not result in MMMs with lower permeabilities as in both cases the gas molecules follow the same path (i.e. going around the filler).

However, after 150 days of physical aging, MMMs prepared using P-H24 exhibit higher CO_2 permeability as compared to P-GO24 at comparable filler loadings. As physical aging continues, the permeability of the polymer phase strongly decays whereas the permeability of the filler remains unaltered. Then, $\dfrac{P_f}{P_p}$ increases and the impact of the filler permeability in Eq. 6 becomes noticeable, so P_f was calculated following the same procedure as for non-porous ODA-GO nanofillers. CO_2 permeabilities ranging from 51 to 379 Barrer and CH_4 permeabilities in the range 1.7 - 21.1 Barrer were obtained. It is worth noting that CO_2 and CH_4 permeabilities found for ODA-HGO are considerably higher than those for P-H24 nanofillers, which explains why the non-(PIM-1) functionalized nanofiller has a greater impact on the gas permeabilities in fresh membranes.

To assess the accuracy of these calculations, the CO_2 and CH_4 permeabilities of MMMs at 0 and 150 days of physical aging were calculated using the Maxwell-Wagner-Sillars equation and plotted in Figure 6. The model can reasonably predict the CO_2 and CH_4

permeabilities of the MMMs having 0.1%, 0.2% and 0.5% ODA-HGO nanofillers at both fresh (t = 0 days) and aged (t = 150 days) conditions (Figure 6a-b). The model exhibits some limitations to forecast the gas permeabilities of (P-H24)-containing MMMs, in particular for CO_2 and for the membrane with the highest loading (Figure 6c). Deviation from the Maxwell model has been widely reported for a wide variety of fillers and is mainly attributed to rigidification effects which are not taken into account in the Maxwell-Wagner-Sillars equation and typically leads to lower gas permeabilities within the polymer phase.[63] This explains the lower CO_2 permeabilities observed in Figure 6c. In fact, throughout this manuscript, as well as in other publications,[27, 28, 52] it has been reported that graphene-based nanofillers exert rigidification on the polymer chains, which is associated with less severe physical aging and lower gas permeabilities for fresh membranes. In this work, it has been found that for MMMs containing P-H24, higher nanofiller loadings result in less physical aging of the polymer due to greater rigidification effects. It is not surprising then that in fresh (P-H24)-containing membranes (shown in Figure 6c) the higher the loading the larger the deviation from the predicted CO_2 permeability. Likewise, Figure 6a shows a notably lower CO_2 permeability for 0.2% ODA-HGO-4h as compared to other loadings. As explained, among all ODA-HGO-4h MMMs, 0.2% ODA-HGO-4h corresponds to the membrane that suffers the lowest CO_2 permeability drop, in other words, less physical aging due to higher rigidification effects. However, deviation from the model can also arise due to the above-mentioned assumptions made to calculate P_f. Therefore, the values reported in this work only represent an estimation of the real P_f and confirm that i) both ODA-HGO and P-H24 permeabilities are much smaller as compared to PIM-1 and ii) the ODA functionalized GO has considerably larger permeability than the PIM-1 functionalized nanofiller.
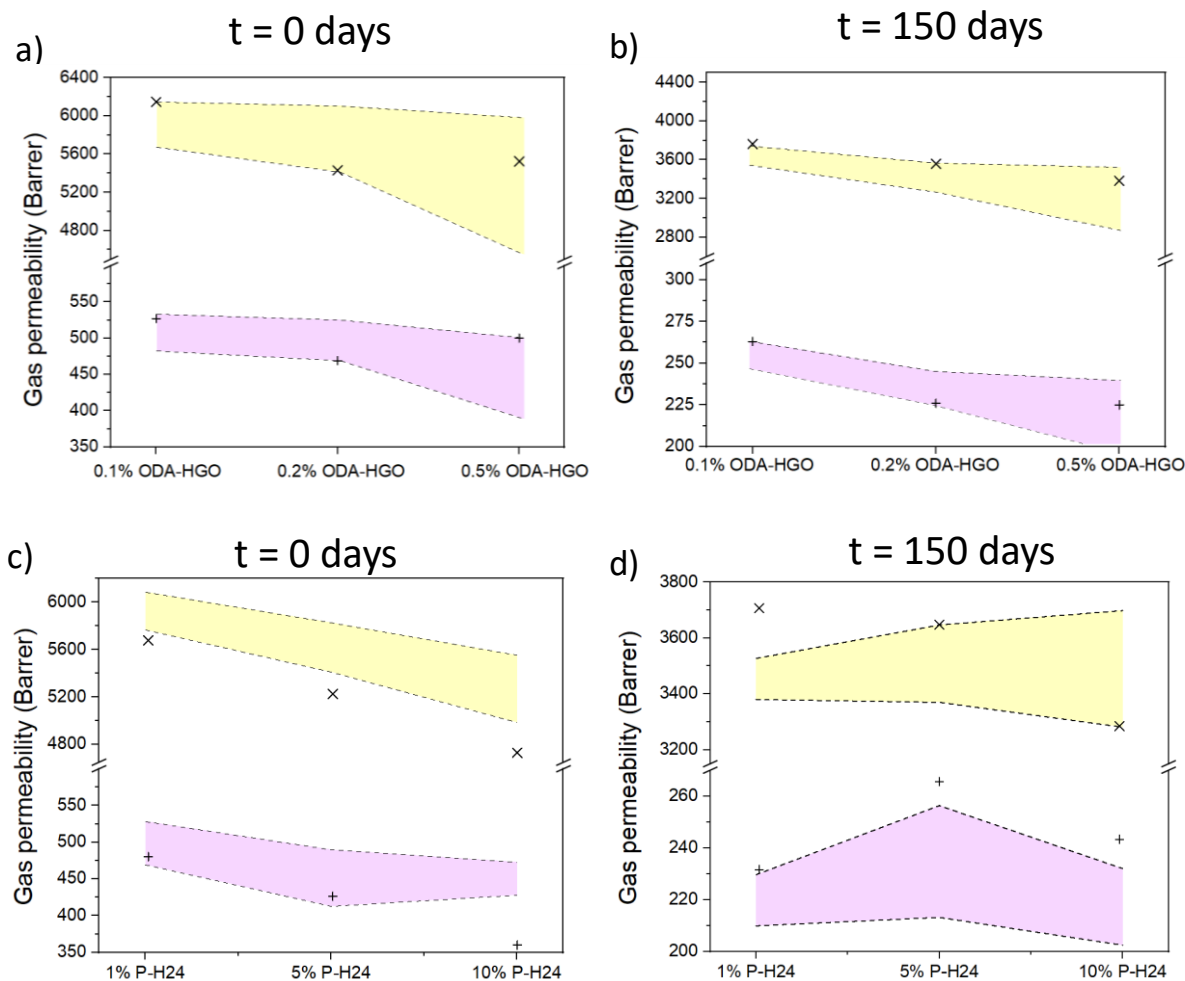
Figure 6. Modelled and experimentally obtained CO_2 and CH_4 permeabilities of MMMs containing ODA-HGO (a and b) and P-H24 (c and d) at 0 and 150 days of physical aging. Light yellow and light purple regions represent the range of CO_2 and CH_4 permeabilities, respectively, predicted by the Maxwell-Wagner-Sillars equation, whereas the rotated (x) and straight (+) crosses correspond to the experimental gas permeability values for each MMM.

3.7. Comparison of the long-term gas separation performance of (PIM-1)-based MMMs

A few other 2D materials, such as exfoliated graphene and boron nitride nanosheets (BNNS), have been also used as nanofillers within PIM-1 matrices. MMMs composed of

PIM-1 and few-layer pristine graphene were prepared (denoted as KA1-7(6) and KA1-7(2)) via ultrasound-assisted exfoliation of natural graphite and subsequent blending with PIM-1.[26] The incorporation of the nanomaterial increased the gas permeability but compromised the gas selectivity and showed only a relative improvement in physical aging mitigation due to a poor dispersion of the nanofiller in the polymer matrix (relative to initial CO_2 permeability ranging from 0.68 to 0.73 for MMMs as compared to 0.72 for PIM-1). 2D boron nitride nanosheets (BNNS) have been also used as nanofillers within PIM-1 matrices with satisfactory gas separation performance after 414 days of physical aging.[52] Being isostructural to graphene, BNNS has been shown to induce rigidification effects on the polymer chains and partially prevent PIM-1 physical aging in a similar manner to graphene-like nanofillers. The most effective membrane in terms of physical aging mitigation contained 0.5 wt % of BNNS and showed a CO_2 permeability drop of 1,293 Barrer, and a relative to initial permeability of 0.78.

Figure 7a shows the Robeson plot of several aged (PIM-1)-based MMMs containing 2D nanofillers and the MMMs presented in this manuscript (highlighted by a yellow-shaded inset). It is important to note that MMMs reported in previous studies (e.g. 0.05% ODA-GO[27] and KA1-7(2)[26]) exhibit better performances than MMMs presented in this manuscript (P-H24 and ODA-HGO-4h), which is due to the higher initial performance of the base polymer; in Figure 7a, a black circle corresponds to PIM-1 measured in this study, whereas a black pentagon and a black hexagon correspond to PIM-1 reported by Alberto et al.[27] and by Althumayri et al.[26], respectively. The discrepancy between the performance of different PIM-1 samples has been deeply studied and it can be concluded that this is related to the different PIM-1 topology,[47] membrane casting[64] and post-fabrication treatment.[65, 66] Figure 7b shows that after 150 days of physical aging, the addition of GO nanofillers, in particular holey (PIM-1)-functionalized GO, P-H24 (red

square and green triangle), and non-porous (PIM-1)-functionalized P-GO24 (pink down-pointing triangle), drives the MMMs towards the 2008 upper bound limit; unfilled symbols correspond to membranes at 0 days of physical aging whereas filled symbols corresponds to membranes aged for 150 days. The enhanced selectivity of the MMMs results in a shift upwards in the Robeson plot, whereas the mitigation of physical aging results in lower CO_2 permeability losses (i.e. lesser shift to the left) than pure PIM-1 membranes (represented by the black circles).
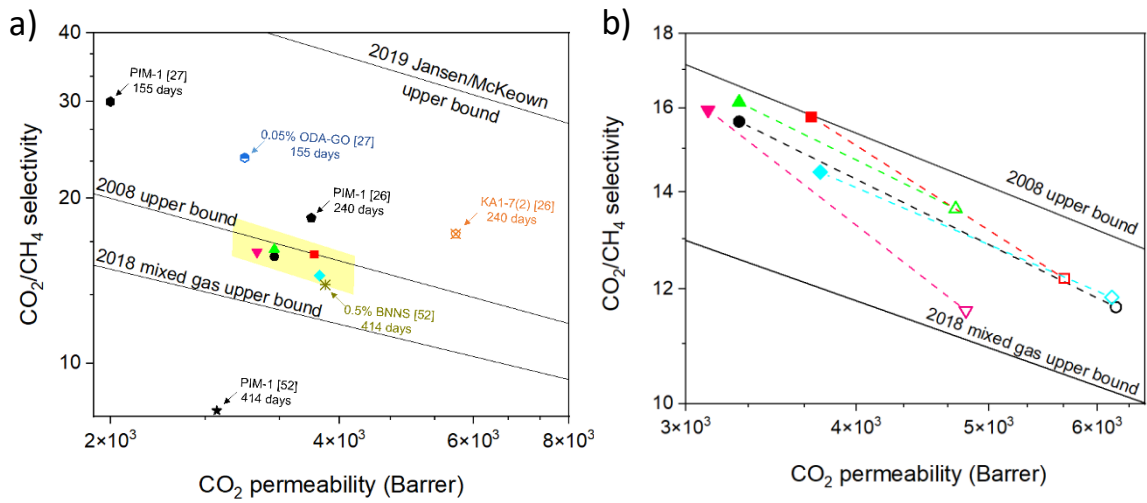
Figure 7. Double logarithmic plot of CO_2/CH_4 selectivities vs. CO_2 permeabilities of membranes containing graphene-like nanofillers where membranes presented in this manuscript are highlighted by a yellow inset (a). Enlarged area of the Robeson plot showing the changes in gas separation performance over time of membranes reported in this manuscript after 150 days of physical aging (b). PIM-1 (○), PIM-1 aged for 150 days (●), 1% P-H24 (□), 1% P-H24 aged for 150 days (■), 10% P-H24 (△), 10% P-H24 aged for 150 days (▲), 0.1% ODA-HGO-4h (◇), 0.1% ODA-HGO-4h aged for 150 days (◆), 10% P-GO24 (▽), 10% P-GO24 aged for 150 days (▼), PIM-1 aged for 155 days (⬣),[27] 0.05% ODA-GO aged for 155 days (⬣),[27] PIM-1 aged for 240 days (⬠),[26] KA1-7(2) aged

38

for 240 days (⊠),[26] PIM-1 aged for 414 days (★)[52] and 0.5% BNNS aged for 414 days (✳).[52]

A large share of gas separation membrane research focuses on high free volume polymers (i.e. superglassy polymers) which show much higher gas permeabilities than other conventionally used glassy polymer materials. However, superglassy polymers like PIM-1 show much faster physical aging, which becomes even faster as their thickness is reduced; for instance, a 200 nm thick PIM-1 membrane showed a 95% CO_2 permeability loss in just less than three months,[67, 68] whereas thick films only lose ~50% of their initial permeability over six months. Furthermore, at industrial scale the preparation of thin film composite (TFC) membranes with a very thin selective layer is necessary to achieve the required product output. For TFCs the gas permeance unit (GPU) is often used rather than the gas permeability unit Barrer. A PIM-1 TFC membrane with a CO_2 permeance of ~5000 GPU that suffers 95% drop of its initial permeability results in a CO_2 permeance of 250 GPU after three months. If the physical aging was mitigated by 30% by the addition of fillers the CO_2 permeance after three months would be 1675 GPU, whereas an improvement in the initial CO_2 permeability, for example a filler that doubles the initial CO_2 permeance (i.e. 10000 GPU) but does not hinder physical aging (95% drop), would end up with a CO_2 permeance of 500 GPU after the same aging period. Therefore, fillers with sizes in the nanometer range with a strong ability to hinder physical aging are desired for the fabrication of TFC PIM-1 membranes. Hence, GO fillers are promising candidates despite decreasing the gas permeation in fresh membranes, and their use in the preparation of TFCs has been reported elsewhere.[21, 32] However, in this study, thick MMMs (~50 μm) were prepared and tested since they are a robust and useful tool to understand how the nanofillers affect the gas permeation and physical aging of polymer membranes, and are therefore, the first step towards the development of commercially relevant TFCs.

Upon the last decade, a wide range of fillers (apart from the discussed 2D materials) have been incorporated into PIM-1 matrices leading to rigidification effects and physical aging prevention. For instance, Lau et al.[29] reported MMMs made of PIM-1 and PAF-1 having a CO_2 permeability of 13,000 Barrer and a relative to initial CO_2 permeability of 0.93 after 150 days. Later, (PIM-1)-functionalized UiO-66-NH$_2$ (a type of metal organic framework) showed a final CO_2 permeability of 10,700 Barrer, a CO_2 permeability drop of 1800 Barrer, and a relative to initial CO_2 permeability of 0.86 after 150 days of physical aging.[24] Despite the outstanding long-term gas separation performance of both PAF-1 and UiO-66-NH$_2$ fillers, they show limited applicability for industrial gas separations since both fillers are of a few microns size, which does not allow the formation of thin film composite (TFC) membranes required for industrial separation processes. Fillers being in the nanometer size such as polyhedral oligomeric silsesquioxane (POSS)[30] and beta-cyclodextrin[31] have also been investigated and offer an acceptable gas separation over 120 days as a result of both enhanced gas permeation and slight mitigation of physical aging. Recently, low cross-link density (LCD) network-PIM-1 materials were incorporated as nanofillers with PIM-1.[69] The prepared MMMs showed an improvement in the initial CO_2 permeability of the membranes; from 5,920 Barrer for PIM-1 to 12,510 Barrer when 15 wt % of nanofiller was added, and a decrease of the physical aging rate (a relative to initial CO_2 permeability of 0.71 that represents a 129% of improvement as compared to PIM-1 itself). The nanofillers used in this manuscript (ODA-HGO-4h and P-H24) have the advantage over the above-mentioned fillers of being atomically thick, which allows the formation of ultrathin MMMs, and at the same time present large lateral size (~ 5 μm average size) being capable of exerting strong rigidification effects on the polymer chains. In addition, the starting material, GO, is commercially available, relatively cheap, highly processable, and can be easily incorporated to the polymer

membrane with minimal modification of the state-of-the-art membrane manufacturing procedures.

4. Conclusions

In this study, we report a strategy to improve the long-term performance of PIM-1 by the addition of holey GO-based nanofillers, and we prove that the chemistry and the porosity of the nanofiller plays an important role in the performance of the MMMs.

After 150 days of physical aging, MMMs containing nanoporous GO nanofillers exhibit higher CO_2 permeabilities and CO_2/CH_4 selectivities than pure PIM-1 membranes and MMMs containing non-porous GO-like materials. The best performing membrane in terms of absolute CO_2 permeability with a loading of 0.1% ODA-HGO-4h shows a 15% higher permeability (~500 Barrer) than that of pure PIM-1.

Chemical functionalization of nanoporous GO with PIM-1 is required to achieve higher loadings of the nanofillers in the polymer matrices, which results in higher physical aging prevention. In terms of permeability drop the best performing membrane (the one with the lowest permeability drop after 150 days of aging) is the one containing 10% of P-H24 (CO_2 permeability drop of 1445 Barrer), which represents half of the permeability drop in PIM-1 without fillers.

In addition, the gas permeability of both nanofillers has been rationalized using the Maxwell-Wagner-Sillars equation and supporting the hypothesis that nanopores in the basal plane of GO contribute to improve the gas permeabilities of the MMMs after 150 days of physical aging. To sum up, the materials presented in this manuscript exhibit particularly promising performance for CO_2 removal from natural gas, although the mitigation of physical aging along with the incorporation of a porous nanofiller make these materials appealing candidates for several applications, including other membrane-

based separations (gas separation, pervaporation, redox flow batteries, etc.), gas and pollutant adsorbents, energy storage, catalysis, and sensing.

Acknowledgments

Supporting information

- Proposed molecular structure of holey graphene oxide (HGO) materials

    o HGO-4h

    o ODA-HGO-4h

- Results

    o XPS characterization of GO, cGO, HGO-4h and HGO-8h.

    o Methylene blue adsorption experiments of GO, cGO, HGO-4h and HGO-8h

    o FT-IR spectra of GO, HGO-4h and ODA-HGO-4h

    o Raman spectra of GO and HGO-4h

    o TEM imaging of GO, cGO, HGO-4h and HGO-8h

- Nuclear magnetic resonance (NMR)

- Elemental analysis of PIM-1, HGO-4h and P-H24

- N_2 sorption characterization of PIM-1 and P-H24

- FT-IR characterization of PIM-1, HGO-4, P-H24 and f-P-H24

- XPS characterization of PIM-1 and f-P-H24

- TGA characterization of PIM-1, HGO-4h, P-H24 and f-P-GO24

- UV-Vis characterization of PIM-1, HGO-4h, P-H24 and f-P-H24

- TEM characterization of PIM-1 and f-P-H24

- SEM characterization of PIM-1 and MMMs containing ODA-HGO-4h and P-H24 nanofillers

- Micrometer measurements of PIM-1 and MMMs containing ODA-HGO-4h and P-H24 nanofillers

- CO_2/CH_4 separation performance of MMMs containing ODA-HGO-4h and P-H24 nanofillers

- Average and standard deviation data corresponding to CO_2 and CH_4 permeability, CO_2/CH_4 selectivity, CO_2 permeability drop and relative CO_2 permeability of PIM-1 and MMMs containing ODA-HGO-4h and P-H24 nanofillers.

- Rationalization of the MMMs gas separation performance using the Maxwell model.

References

1.   Adewole, J. K.; Ahmad, A. L.; Ismail, S.; Leo, C. P., Current Challenges in Membrane Separation of CO2 from Natural Gas: A Review. *Int. J. Greenh. Gas Con.* **2013,** *17,* 46-65.

2.   Rufford, T. E.; Smart, S.; Watson, G. C. Y.; Graham, B. F.; Boxall, J.; da Costa, J. C. D.; May, E. F., The removal of CO2 and N-2 from natural gas: A review of conventional and emerging process technologies. *J. Petrol. Sci. Eng.* **2012,** *94-95*, 123-154.

3.   Scholz, M.; Melin, T.; Wessling, M., Transforming biogas into biomethane using membrane technology. *Renew. Sust. Energ. Rev.* **2013,** *17*, 199-212.

4.   Scholes, C. A.; Stevens, G. W.; Kentish, S. E., Membrane gas separation applications in natural gas processing. *Fuel* **2012,** *96* (1), 15-28.

5.   Bernardo, P.; Drioli, E.; Golemme, G., Membrane Gas Separation: A Review/State of the Art. *Ind. Eng. Chem. Res.* **2009,** *48* (10), 4638-4663.

6.   Sanders, D. E.; Smith, Z. P.; Guo, R.; Robeson, L. M.; McGrath, J. E.; Paul, D. R.; Freeman, B. D., Energy-efficient polymeric gas separation membranes for a sustainable future: A review. *Polymer* **2013,** *54* (18), 4729-4761.

7.   White, L., Evolution of natural gas treatment with membrane systems. In *Membrane gas separation*, John Wiley & Sons: Singapore, 2010; pp 313–32.

8.   Galizia, M.; Chi, W. S.; Smith, Z. P.; Merkel, T. C.; Baker, R. W.; Freeman, B. D., 50th Anniversary Perspective: Polymers and Mixed Matrix Membranes for Gas and Vapor Separation: A Review and Prospective Opportunities. *Macromolecules* **2017,** *50* (20), 7809-7843.

9.   McKeown, N. B.; Budd, P. M., Polymers of intrinsic microporosity (PIMs): organic materials for membrane separations, heterogeneous catalysis and hydrogen storage. *Chem. Soc. Rev.* **2006,** *35* (8), 675-683.

10.   Budd, P. M.; McKeown, N. B., Highly permeable polymers for gas separation membranes. *Polym. Chem.* **2010,** *1* (1), 63-68.

11.   Budd, P. M.; Msayib, K. J.; Tattershall, C. E.; Ghanem, B. S.; Reynolds, K. J.; McKeown, N. B.; Fritsch, D., Gas separation membranes from polymers of intrinsic microporosity. *J. Membr. Sci.* **2005,** *251* (1-2), 263-269.

12.   Robeson, L. M.; Dose, M. E.; Freeman, B. D.; Paul, D. R., Analysis of the transport properties of thermally rearranged (TR) polymers and polymers of intrinsic microporosity (PIM) relative to upper bound performance. *J. Membr. Sci.* **2017,** *525*, 18-24.

13.   Carta, M.; Malpass-Evans, R.; Croad, M.; Rogan, Y.; Jansen, J. C.; Bernardo, P.; Bazzarelli, F.; McKeown, N. B., An efficient polymer molecular sieve for membrane gas separations. *Science* **2013,** *339* (6117), 303-307.

14.   Low, Z. X.; Budd, P. M.; McKeown, N. B.; Patterson, D. A., Gas permeation properties, physical aging, and its mitigation in high free volume glassy polymers. *Chem. Rev.* **2018,** *118* (12), 5871-5911.

15.   Kim, H. J.; Kim, D. G.; Lee, K.; Baek, Y.; Yoo, Y.; Kim, Y. S.; Kim, B. G.; Lee, J. C., A carbonaceous membrane based on a polymer of intrinsic microporosity (PIM-1) for water treatment. *Sci. Rep.* **2016,** *6*.

16.   Wang, L. N.; Zhao, Y. Z.; Fan, B. B.; Carta, M.; Malpass-Evans, R.; McKeown, N. B.; Marken, F., Polymer of intrinsic microporosity (PIM) films and membranes in electrochemical energy storage and conversion: A mini-review. *Electrochem. commun.* **2020,** *118*.

17.   Molefe, L. Y.; Musyoka, N. M.; Ren, J. W.; Langmi, H. W.; Mathe, M.; Ndungu, P. G., Effect of Inclusion of MOF-Polymer Composite onto a Carbon Foam Material for Hydrogen Storage Application. *J. Inorg. Organomet. Polym. Mater.* **2021,** *31* (1), 80-88.

18.   Wang, S.; Pomerantz, N. L.; Dai, Z.; Xie, W.; Anderson, E. E.; Miller, T.; Khan, S. A.; Parsons, G. N., Polymer of intrinsic microporosity (PIM) based fibrous mat:

combining particle filtration and rapid catalytic hydrolysis of chemical warfare agent simulants into a highly sorptive, breathable, and mechanically robust fiber matrix. *Mater. Today Adv.* **2020,** *8*.

19.   Jahani, N.; Amiri, M.; Ghiasi, M.; Imanzadeh, H.; Boukherroub, R.; Szunerits, S.; Marken, F.; McKeown, N. B., Non-enzymatic electrochemical cholesterol sensor based on strong host-guest interactions with a polymer of intrinsic microporosity (PIM) with DFT study. *Anal. Bioanal. Chem.*

20.   Alberto, M.; Luque-Alled, J. M.; Gao, L.; Iliut, M.; Prestat, E.; Newman, L.; Haigh, S. J.; Vijayaraghavan, A.; Budd, P. M.; Gorgojo, P., Enhanced organophilic separations with mixed matrix membranes of polymers of intrinsic microporosity and graphene-like fillers. *J. Membr. Sci.* **2017,** *526*, 437-449.

21.   Alberto, M.; Bhavsar, R.; Luque-Alled, J. M.; Prestat, E.; Gao, L.; Budd, P. M.; Vijayaraghavan, A.; Szekely, G.; Holmes, S. M.; Gorgojo, P., Study on the formation of thin film nanocomposite (TFN) membranes of polymers of intrinsic microporosity and graphene-like fillers: Effect of lateral flake size and chemical functionalization. *J. Membr. Sci.* **2018,** *565*, 390-401.

22.   Alammar, A.; Park, S. H.; Ibrahim, I.; Arun, D.; Holtzl, T.; Dumee, L. F.; Lim, H. N.; Szekely, G., Architecting neonicotinoid-scavenging nanocomposite hydrogels for environmental remediation. *Appl. Mater. Today* **2020,** *21*.

23.   Rong, Y.; Large, M. J.; Tripathi, M.; Ogilvie, S. P.; Amorim Graf, A.; Mao, B.; Tunesi, J.; Salvage, J. P.; King, A. A. K.; Pasquazi, A.; Peccianti, M.; Malpass-Evans, R.; McKeown, N. B.; Marken, F.; Dalton, A. B., Charge transfer hybrids of graphene oxide and the intrinsically microporous polymer PIM-1. *ACS Appl. Mater. Inter.* **2019,** *11* (34), 31191-31199.

24. Nguyen, T. B.; Rodrigue, D.; Kaliaguine, S., In-situ cross interface linking of PIM-1 polymer and UiO-66-NH2 for outstanding gas separation and physical aging control. *J. Membr. Sci.* **2018,** *548*, 429-438.

25. Tamaddondar, M.; Foster, A. B.; Luque-Alled, J. M.; Msayib, K. J.; Carta, M.; Sorribas, S.; Gorgojo, P.; McKeown, N. B.; Budd, P. M., Intrinsically Microporous Polymer Nanosheets for High-Performance Gas Separation Membranes. *Macromol. Rapid Commun.* **2020,** *41* (2), 8.

26. Althumayri, K.; Harrison, W. J.; Shin, Y.; Gardiner, J. M.; Casiraghi, C.; Budd, P. M.; Bernardo, P.; Clarizia, G.; Jansen, J. C., The influence of few-layer graphene on the gas permeability of the high-free-volume polymer PIM-1. *Philos. Trans. Royal Soc. A* **2016,** *374* (2060).

27. Alberto, M.; Bhavsar, R.; Luque-Alled, J. M.; Vijayaraghavan, A.; Budd, P. M.; Gorgojo, P., Impeded physical aging in PIM-1 membranes containing graphene-like fillers. *J. Membr. Sci.* **2018,** *563*, 513-520.

28. Luque-Alled, J. M.; Ameen, A. W.; Alberto, M.; Tamaddondar, M.; Foster, A. B.; Budd, P. M.; Vijayaraghavan, A.; Gorgojo, P., Gas separation performance of MMMs containing (PIM-1)-functionalized GO derivatives. *J. Membr. Sci.* **2021,** *623*.

29. Lau, C. H.; Nguyen, P. T.; Hill, M. R.; Thornton, A. W.; Konstas, K.; Doherty, C. M.; Mulder, R. J.; Bourgeois, L.; Liu, A. C. Y.; Sprouster, D. J.; Sullivan, J. P.; Bastow, T. J.; Hill, A. J.; Gin, D. L.; Noble, R. D., Ending aging in super glassy polymer membranes. *Angwe. Chem. Int. Ed.* **2014,** *53* (21), 5322-5326.

30. Yong, W. F.; Kwek, K. H. A.; Liao, K. S.; Chung, T. S., Suppression of aging and plasticization in highly permeable polymers. *Polymer* **2015,** *77*, 377-386.

31. Liu, J. T.; Xiao, Y. C.; Liao, K. S.; Chung, T. S., Highly permeable and aging resistant 3D architecture from polymers of intrinsic microporosity incorporated with beta-cyclodextrin. *J. Membr. Sci.* **2017,** *523*, 92-102.

32. Aliyev, E. M.; Khan, M. M.; Nabiyev, A. M.; Alosmanov, R. M.; Bunyad-zadeh, I. A.; Shishatskiy, S.; Filiz, V., Covalently Modified Graphene Oxide and Polymer of Intrinsic Microporosity (PIM-1) in Mixed Matrix Thin-Film Composite Membranes. *Nanoscale Res. Lett.* **2018,** *13*, 13.

33. Li, X. Q.; Ma, L.; Zhang, H. Y.; Wang, S. F.; Jiang, Z. Y.; Guo, R. L.; Wu, H.; Cao, X. Z.; Yang, J.; Wang, B. Y., Synergistic effect of combining carbon nanotubes and graphene oxide in mixed matrix membranes for efficient CO2 separation. *J. Membr. Sci.* **2015,** *479*, 1-10.

34. Dong, G. Y.; Hou, J. W.; Wang, J.; Zhang, Y. T.; Chen, V.; Liu, J. D., Enhanced CO2/N-2 separation by porous reduced graphene oxide/Pebax mixed matrix membranes. *J. Membr. Sci.* **2016,** *520*, 860-868.

35. Du, N. Y.; Song, J. S.; Robertson, G. P.; Pinnau, I.; Guiver, M. D., Linear high molecular weight ladder polymer via fast polycondensation of 5,5',6,6'-tetrahydroxy-3,3,3',3'-tetramethylspirobisindane with 1,4-dicyanotetrafluorobenzene. *Macromol. Rapid Commun.* **2008,** *29* (10), 783-788.

36. Rourke, J. P.; Pandey, P. A.; Moore, J. J.; Bates, M.; Kinloch, I. A.; Young, R. J.; Wilson, N. R., The real graphene oxide revealed: Stripping the oxidative debris from the graphene-like sheets. *Angwe. Chem. Int. Ed.* **2011,** *50* (14), 3173-3177.

37. Xu, Y. X.; Chen, C. Y.; Zhao, Z. P.; Lin, Z. Y.; Lee, C.; Xu, X.; Wang, C.; Huang, Y.; Shakir, M. I.; Duan, X. F., Solution Processable Holey Graphene Oxide and Its Derived Macrostructures for High-Performance Supercapacitors. *Nano Lett.* **2015,** *15* (7), 4605-4610.

38.   Xu, Y. X.; Lin, Z. Y.; Zhong, X.; Huang, X. Q.; Weiss, N. O.; Huang, Y.; Duan, X. F., Holey graphene frameworks for highly efficient capacitive energy storage. *Nat. Commun.* **2014,** *5*.

39.   Pei, S.; Cheng, H. M., The Reduction of Graphene Oxide. *Carbon* **2012,** *50* (9), 3210.

40.   Huang, S. Q.; Dakhchoune, M.; Luo, W.; Oveisi, E.; He, G. W.; Rezaei, M.; Zhao, J.; Alexander, D. T. L.; Zuttel, A.; Strano, M. S.; Agrawal, K. V., Single-layer graphene membranes by crack-free transfer for gas mixture separation. *Nat. Commun.* **2018,** *9*.

41.   Leaper, S.; Abdel-Karim, A.; Faki, B.; Luque-Alled, J. M.; Alberto, M.; Vijayaraghavan, A.; Holmes, S. M.; Szekely, G.; Badawy, M. I.; Shokri, N.; Gorgojo, P., Flux-enhanced PVDF mixed matrix membranes incorporating APTS-functionalized graphene oxide for membrane distillation. *J. Membr. Sci.* **2018,** *554*, 309-323.

42.   Montes-Navajas, P.; Asenjo, N. G.; Santamaria, R.; Menendez, R.; Corma, A.; Garcia, H., Surface Area Measurement of Graphene Oxide in Aqueous Solutions. *Langmuir* **2013,** *29* (44), 13443-13448.

43.   Alsharaeh, E.; Ahmed, F.; Aldawsari, Y.; Khasawneh, M.; Abuhimd, H.; Alshahrani, M., Novel synthesis of holey reduced graphene oxide (HRGO) by microwave irradiation method for anode in lithium-ion batteries. *Sci. Rep.* **2016,** *6*.

44.   Bai, Y. L.; Yang, X. F.; He, Y. B.; Zhang, J. Y.; Kang, L. P.; Xu, H.; Shi, F.; Lei, Z. B.; Liu, Z. H., Formation process of holey graphene and its assembled binder-free film electrode with high volumetric capacitance. *Electrochim. Acta* **2016,** *187*, 543-551.

45.   Dimiev, A. M.; Tour, J. M., Mechanism of Graphene Oxide Formation. *Acs Nano* **2014,** *8* (3), 3060-3068.

46.   Song, Q. L.; Cao, S.; Pritchard, R. H.; Qiblawey, H.; Terentjev, E. M.; Cheetham, A. K.; Sivaniah, E., Nanofiller-tuned microporous polymer molecular sieves for energy and environmental processes. *J. Mater. Chem. A* **2016,** *4* (1), 270-279.

47.   Foster, A. B.; Tamaddondar, M.; Luque-Alled, J. M.; Harrison, W. J.; Li, Z.; Gorgojo, P.; Budd, P. M., Understanding the Topology of the Polymer of Intrinsic Microporosity PIM-1: Cyclics, Tadpoles, and Network Structures and Their Impact on Membrane Performance. *Macromolecules* **2020,** *53* (231), 569-583.

48.   Cheng, Y. D.; Wang, X. R.; Jia, C. K.; Wang, Y. X.; Zhai, L. Z.; Wang, Q.; Zhao, D., Ultrathin mixed matrix membranes containing two-dimensional metal-organic framework nanosheets for efficient CO2/CH4 separation. *J. Membr. Sci.* **2017,** *539*, 213-223.

49.   Perez, E. V.; Balkus, K. J.; Ferraris, J. P.; Musselman, I. H., Mixed-matrix membranes containing MOF-5 for gas separations. *J. Membr. Sci.* **2009,** *328* (1-2), 165-173.

50.   Xin, Q. P.; Li, Z.; Li, C. D.; Wang, S. F.; Jiang, Z. Y.; Wu, H.; Zhang, Y.; Yang, J.; Cao, X. Z., Enhancing the CO2 separation performance of composite membranes by the incorporation of amino acid-functionalized graphene oxide. *J. Mater. Chem. A* **2015,** *3* (12), 6629-6641.

51.   van Essen, M.; Thur, R.; Houben, M.; Vankelecom, I. F. J.; Borneman, Z.; Nijmeijer, K., Tortuous mixed matrix membranes: A subtle balance between microporosity and compatibility. *J. Membr. Sci.* **2021,** *635*, 10.

52.   Ameen, A. W.; Ji, J.; Tamaddondar, M.; Moshenpour, S.; Foster, A. B.; Fan, X.; Budd, P. M.; Mattia, D.; Gorgojo, P., 2D boron nitride nanosheets in PIM-1 membranes for CO_2/CH_4 separation. *J. Membr. Sci.* **2021**.

53.   Foster, A. B.; Beal, J. L.; Tamaddondar, M.; Luque-Alled, J. M.; Robertson, B.; Mathias, M.; Gorgojo, P.; Budd, P. M., Importance of small loops within PIM-1 topology on gas separation selectivity in thin film composite membranes. *J. Mater. Chem. A*.

54.   Guo, H.; Liu, J. Q.; Li, Y. H.; Caro, J.; Huang, A. S., Post-synthetic modification of highly stable UiO-66-NH2 membranes on porous ceramic tubes with enhanced H-2 separation. *Micropor. Mesopour. Mater.* **2021,** *313*.

55.   Huang, A. S.; Wang, N. Y.; Kong, C. L.; Caro, J., Organosilica-Functionalized Zeolitic Imidazolate Framework ZIF-90 Membrane with High Gas-Separation Performance. *Angwe. Chem. Int. Ed.* **2012,** *51* (42), 10551-10555.

56.   Ray, P.; Gidley, D.; Badding, J. V.; Lueking, A. D., UV and chemical modifications of polymer of Intrinsic Microporosity 1 to develop vibrational spectroscopic probes of surface chemistry and porosity. *Micropor. Mesopour. Mater.* **2019,** *277*, 29-35.

57.   Liu, M.; Lu, X. X.; Nothling, M. D.; Doherty, C. M.; Zu, L. H.; Hart, J. N.; Webley, P. A.; Jin, J. Y.; Fu, Q.; Qiao, G. G., Physical Aging Investigations of a Spirobisindane-Locked Polymer of Intrinsic Microporosity. *ACS Mater. Lett.* **2020,** *2* (8), 993-998.

58.   McDermott, A. G.; Budd, P. M.; McKeown, N. B.; Colina, C. M.; Runt, J., Physical aging of polymers of intrinsic microporosity: a SAXS/WAXS study. *J. Mater. Chem. A* **2014,** *2* (30), 11742-11752.

59.   Lau, C. H.; Konstas, K.; Thornton, A. W.; Liu, A. C. Y.; Mudie, S.; Kennedy, D. F.; Howard, S. C.; Hill, A. J.; Hill, M. R., Gas-Separation Membranes Loaded with Porous Aromatic Frameworks that Improve with Age. *Angwe. Chem. Int. Ed.* **2015,** *54* (9), 2669-2673.

60.   Monsalve-Bravo, G. M.; Bhatia, S. K., Modeling Permeation through Mixed-Matrix Membranes: A Review. *Processes* **2018,** *6* (9).

61.   Vu, D. Q.; Koros, W. J.; Miller, S. J., Mixed matrix membranes using carbon molecular sieves - II. Modeling permeation behavior. *J. Membr. Sci.* **2003,** *211* (2), 335-348.

62.   Bouma, R. H. B.; Checchetti, A.; Chidichimo, G.; Drioli, E., Permeation through a heterogeneous membrane: The effect of the dispersed phase. *J. Membr. Sci.* **1997,** *128* (2), 141-149.

63.   Gheimasi, K. M.; Mohammadi, T.; Bakhtiari, O., Modification of ideal MMMs permeation prediction models: Effects of partial pore blockage and polymer chain rigidification. *J. Membr. Sci.* **2013,** *427*, 399-410.

64.   Li, P.; Chung, T. S.; Paul, D. R., Gas sorption and permeation in PIM-1. *J. Membr. Sci.* **2013,** *432*, 50-57.

65.   Tocci, E.; De Lorenzo, L.; Bernardo, P.; Clarizia, G.; Bazzarelli, F.; McKeown, N. B.; Carta, M.; Malpass-Evans, R.; Friess, K.; Pilnacek, K.; Lanc, M.; Yampolskii, Y. P.; Strarannikova, L.; Shantarovich, V.; Mauri, M.; Jansen, J. C., Molecular Modeling and Gas Permeation Properties of a Polymer of Intrinsic Microporosity Composed of Ethanoanthracene and Troger's Base Units. *Macromolecules* **2014,** *47* (22), 7900-7916.

66.   Budd, P. M.; McKeown, N. B.; Ghanem, B. S.; Msayib, K. J.; Fritsch, D.; Starannikova, L.; Belov, N.; Sanfirova, O.; Yampolskii, Y.; Shantarovich, V., Gas permeation parameters and other physicochemical properties of a polymer of intrinsic microporosity: Polybenzodioxane PIM-1. *J. Membr. Sci.* **2008,** *325* (2), 851-860.

67.   Borisov, I.; Bakhtin, D.; Luque-Alled, J. M.; Rybakova, A.; Makarova, V.; Foster, A. B.; Harrison, W. J.; Volkov, V.; Polevaya, V.; Gorgojo, P.; Prestat, E.;

Budd, P. M.; Volkov, A., Synergistic enhancement of gas selectivity in thin film composite membranes of PIM-1. *J. Mater. Chem. A* **2019,** *7* (11), 6417-6430.

68.   Tiwari, R. R.; Jin, J. Y.; Freeman, B. D.; Paul, D. R., Physical aging, CO2 sorption and plasticization in thin films of polymer with intrinsic microporosity (PIM-1). *J. Membr. Sci.* **2017,** *537*, 362-371.

69.   Tamaddondar, M.; Foster, A. B.; Carta, M.; Gorgojo, P.; McKeown, N. B.; Budd, P. M., Mitigation of Physical Aging with Mixed Matrix Membranes Based on Cross-Linked PIM-1 Fillers and PIM-1. *ACS Appl. Mater. Inter.* **2020,** *12* (41), 46756-46766.

For Table of Contents Only
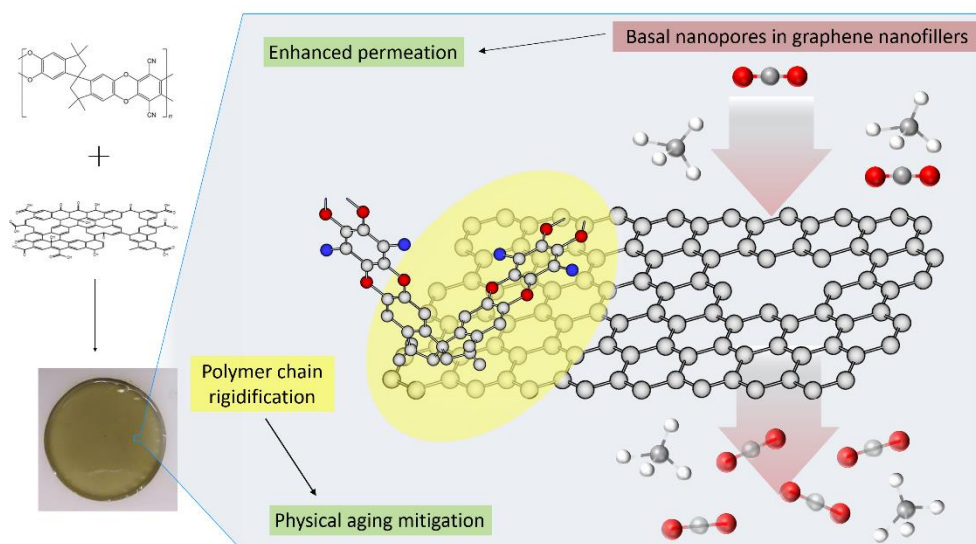
Supporting Information

PIM-1/holey GO mixed matrix membranes for gas separation: unveiling the role of holes

Jose Miguel Luque-Alled [a], Marzieh Tamaddondar [b], Andrew B. Foster [b], Peter M. Budd [b], Patricia Gorgojo [a,c,d]*

[a] Department of Chemical Engineering and Analytical Science, School of Engineering, The University of Manchester, Oxford Road, Manchester, M13 9PL, United Kingdom

[b] Department of Chemistry, School of Natural Sciences, The University of Manchester, Oxford Road, Manchester, M13 9PL, United Kingdom

[c] Nanoscience and Materials Institute of Aragón (INMA) CSIC-Universidad de Zaragoza, C/ Mariano Esquillor s/n, 50018 Zaragoza, Spain

[d] Chemical and Environmental Engineering Department, Universidad de Zaragoza, C/ Pedro Cerbuna 12, 50009 Zaragoza, Spain

* Corresponding author:

p.gorgojo@manchester.ac.uk (P. Gorgojo)

1. Proposed molecular structure of holey graphene oxide (HGO) materials
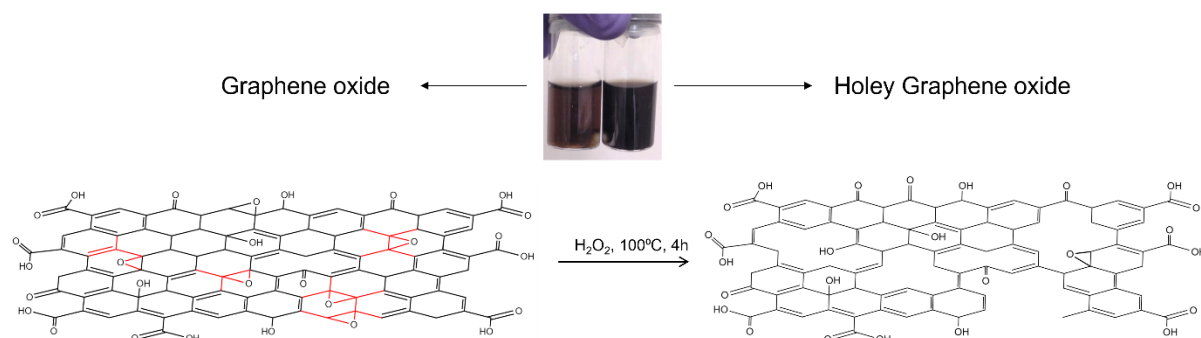
1.1. HGO-4h

Figure S1. Schematic representation of HGO-4h formation. Carbon atoms undergoing oxidation reactions and further cleavage from the 2D structure are highlighted in red in the GO structure for ease of visualization. Photographs of both GO and HGO-4h dispersions are also included. HGO-4h shows a darker color than GO, which is related to the removal of oxygen functional groups.[1-2]
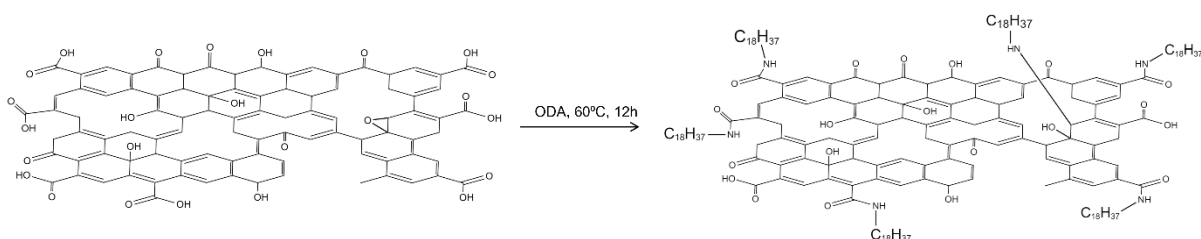
1.2. ODA-HGO-4h

Figure S2. Schematic representation of functionalized-holey GO (ODA-HGO-4h). Nucleophilic substitutions occurring between the amine in ODA and functional groups present in HGO-4h can be clearly observed.

2. Results

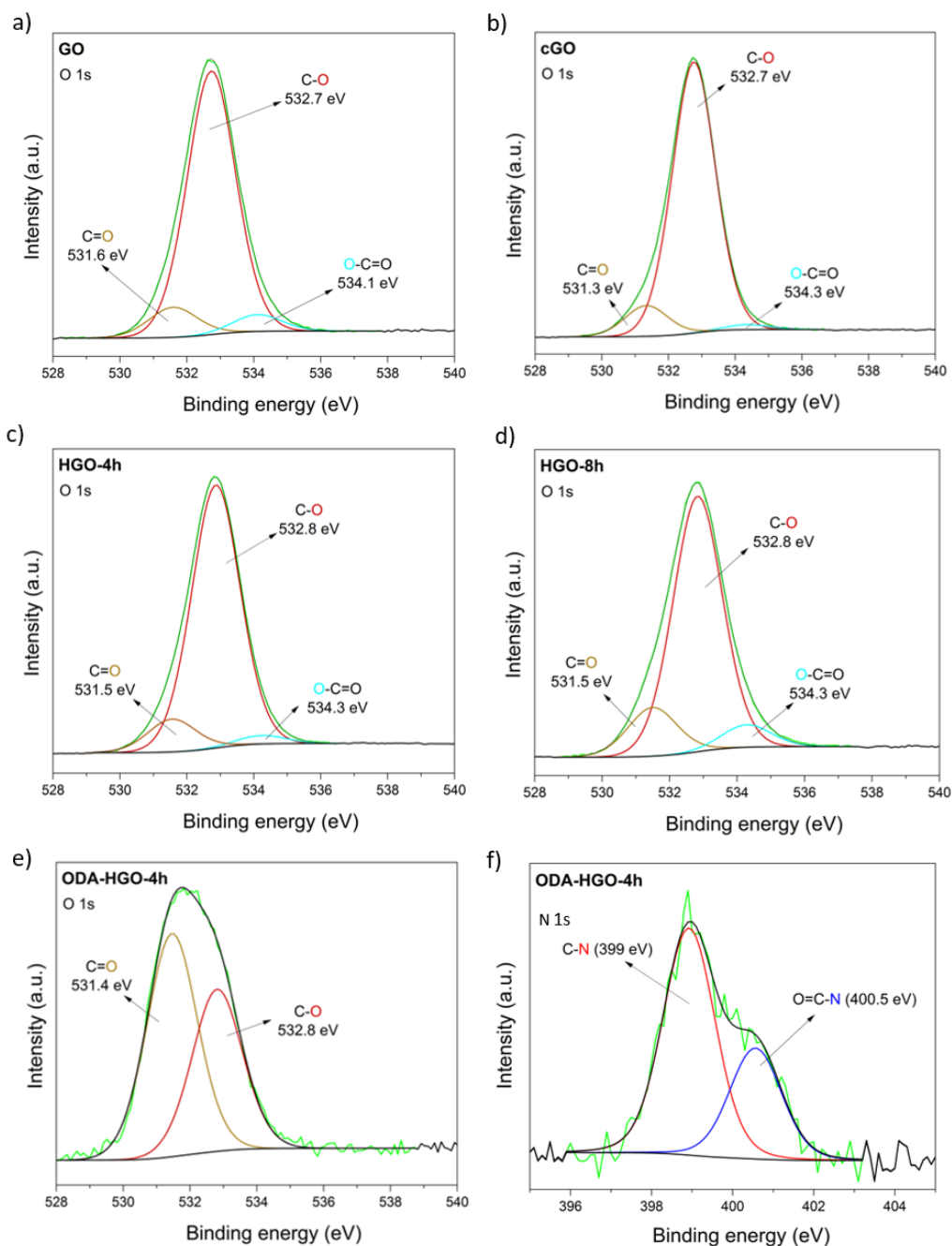## 2.1. XPS characterization of GO, cGO, HGO-4h and HGO-8h.

Figure S3. O1s high resolution XPS spectra of GO (a), cGO (b), HGO-4h (c), HGO-8h (d) and ODA-HGO-4h (e), and N1s high resolution XPS spectra of ODA-HGO-4h (f). In all the XPS spectra, the green line represents the acquired XPS signal, whereas the black line corresponds to the fitted spectrum which includes the contributions of all the individual peaks.

As HGO-4 consists of C and O, it can be assumed that all the N content in the resulting material from the ODA functionalization reaction (i.e. ODA-HGO-4h) comes from the functionalizing agent ODA. Hence, the amount of functionalizing agent incorporated to HGO-4h was estimated using the theoretical weight ratio of ODA. The following table (Table S1) shows the atomic % of each element.

Table S1. Atomic % of GO, cGO, HGO-4h, HGO-8h and ODA-HGO-4h obtained from high resolution XPS measurements.

Sample	%C	%N	%O
GO	69.8	-	30.2
cGO	70.8	-	29.2
HGO-4h	71.7	-	28.3
HGO-8h	72.5	-	27.5
ODA-HGO-4h	89.8	3	7.2

2.2. Methylene blue adsorption experiments of GO, cGO, HGO-4h and HGO-8h

Assuming that 1 mg of methylene blue (MB) corresponds to 2.54 m^2, the surface area of GO or GO derivatives can be estimated by determining the amount of MB adsorbed by the graphene-like material. Therefore, 2.21 mL of MB solution (2 mg mL^{-1}) was added over 5 mg of GO (or GO derivatives) dispersed in 7.79 mL of DI water. After stirring for 24 h, the sample was left to precipitate for 12 h and then the supernatant containing non-adsorbed MB was separated from the precipitate (i.e. MB adsorbed to the graphene-like material) by centrifugation (1000 rpm, 5 min). The supernatant was analyzed by UV-Vis absorption (665

nm) in order to find out the amount of free MB and at the same time allowing the calculation

of the adsorbed MB by the GO (or the GO derivative). For the preparation of the experiments,

the amount of MB added to the GO (or GO derivative) solution was 1.5 times the amount of

MB that corresponds to the theoretical area of graphene (2250 m^2 g^{-1}), which is the

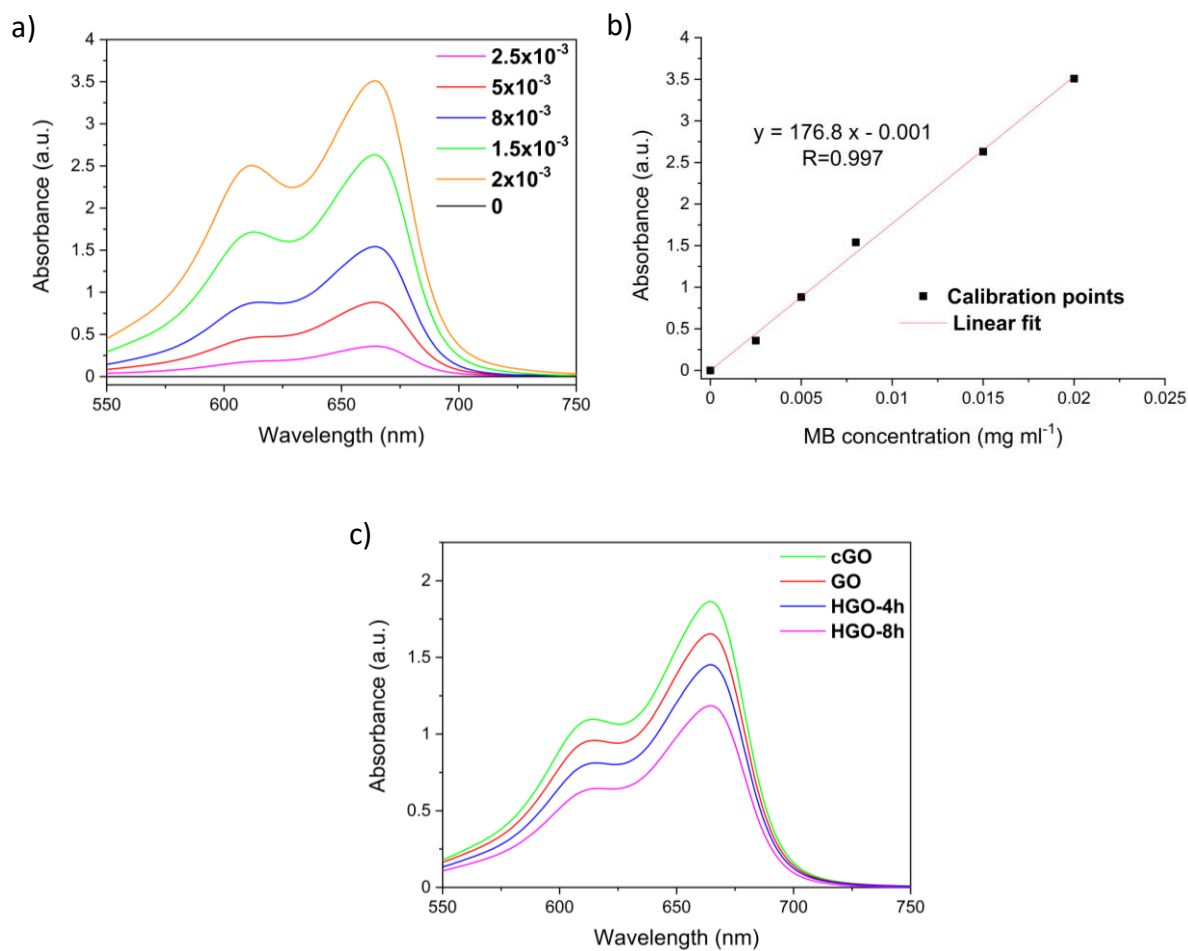conventional MB/GO ratio according to most studies found in the literature.[1, 3]

Figure S4. Methylene Blue (MB) absorbance curves at different MB concentrations (mg ml^{-1})

in water (a), MB linear fit at 665 nm (b) and absorbance measurement of supernatant from

MB/graphene dispersions (c).

2.3. FT-IR spectra of GO, HGO-4h and ODA-HGO-4h

The FT-IR spectrum of HGO-4h shows similar vibrations to that of GO, i.e. epoxide (1040 cm^{-1}), aromatic moieties (1600 cm^{-1}), carbonyl (1720 cm^{-1}) and hydroxyl groups (3300 cm^{-1}).[4-6] However, the peak corresponding to hydroxyl groups (3300 cm^{-1}) seems slightly diminished in the spectrum of HGO-4h, suggesting the removal of the oxygen-containing functional groups. In the HGO-4h spectrum it is also perceptible that the carbonyl peak (1720 cm^{-1}) is slightly more intense than that of GO as a result of the oxidation process and consequent carboxyl and lactone formation.[7-8] The FT-IR spectrum of ODA-HGO-4h exhibits several differences with that of HGO-4h. A new peak at 1460 cm^{-1} corresponding to C-N stretching vibrations arises for ODA-HGO-4h.[9] The peak at 1590 cm^{-1}, attributed to C=C in HGO-4h (1600 cm^{-1}), is broader after ODA functionalization due to the contribution of O=C-N stretching bonding vibrations (typically ~1700 cm^{-1}).[5-6, 9] The peak corresponding to C=O (1720 cm^{-1}) in the spectrum of HGO-4h has almost disappeared in that of ODA-HGO-4h, which is explained by a position shift toward lower wavenumbers and overlapping with the C=C peak due to amide formation as above-mentioned. In addition, two intense peaks corresponding to CH$_2$ and CH$_3$ emerge at 2800-2900 cm^{-1}.[5, 9]
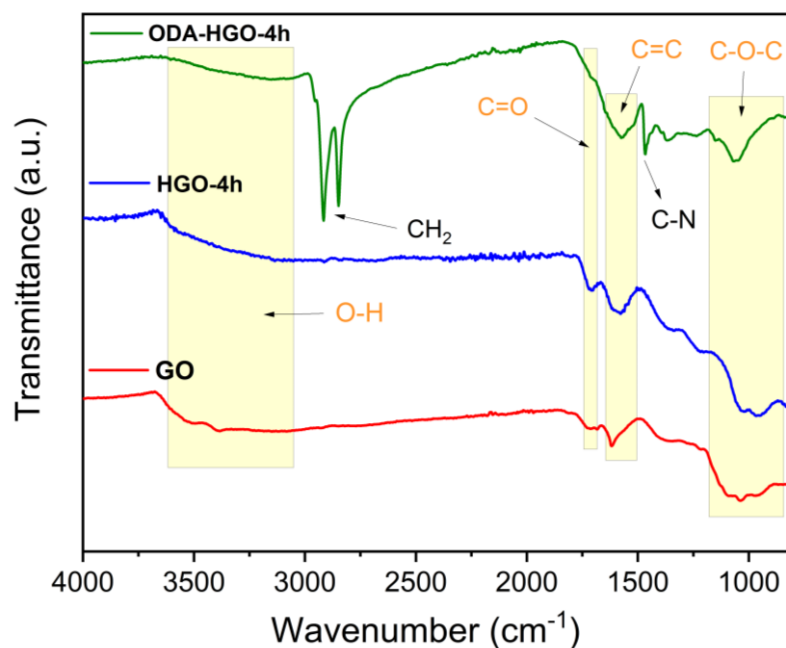
Figure S5. FT-IR spectra of GO, HGO-4h and ODA-HGO-4h. Dim yellow insets indicate the position of all the peaks observed for GO, HGO-4h and ODA-HGO-4h.

2.4. Raman spectra of GO and HGO-4h

The two so-called "G" and "D" peaks are observed in both spectra. The peak at higher wavenumbers around 1600 cm^{-1} (G peak) is characteristic of graphitic structures and corresponds to a first order process arising from the scattering of an incident photon with the vibration modes of graphitic structures. However, the commonly known "D" peak around 1350 cm^{-1} arises from a second order process and is related to the existence of "defects" (e.g. sp^3 carbon atoms and holes/edges) in the graphene layer. The ratio between the intensity of these two peaks (I(D)/I(G)) is often employed to characterize the number of defects in the graphene-like materials. Therefore, it can be expected that HGO-4h shows a higher I(D)/I(G) ratio than GO as a consequence of the oxidation process and hole formation. Nevertheless, the opposite scenario is observed for the samples measured in this manuscript, i.e. a slightly higher I(D)/I(G) in GO than in HGO-4h is obtained from the spectra depicted in Figure S6. This has also been reported by several other authors,[1, 10] and a few facts can explain these observations: i) even

though the graphitic structure may also be affected during the oxidation process, most of the reactions are carried out in the oxygen-containing functional groups since they are more labile. Thus, oxidation of oxygen-containing functional groups will mainly remove sp^3 carbon atoms, reducing the number of functional groups contributing to the D peak.[1, 3] ii) in graphene-like structures with low density of defects, a new peak denoted as D', also due to the presence of defects but different from the D peak, is typically observed at approximately 1620 cm^{-1}. However, when a high density of defects is present, as happens in GO, the G (1600 cm^{-1}) and D' peak become indistinguishable and merge into one main peak ("apparent" G peak),[11] and then it is widely accepted for GO and its derivatives to omit the D' peak, considering only the "apparent" G band.[12-13] Thus, an increase in the number of defects in GO also increases the intensity of the "apparent" G peak (i.e. G + D'). In addition, the D' peak is more intense when atom vacancies are created rather than through the formation of sp^3 carbon atoms and thus the conversion of sp^3 carbons into holes as a result of the oxidation reactions is expected to increase the intensity of the D' peak.[11]
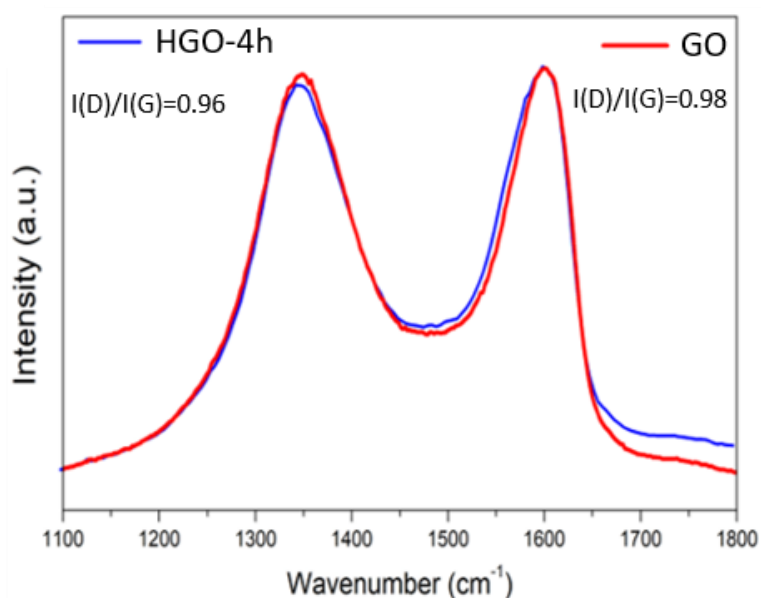

Figure S6. Raman spectra of GO and HGO-4h. Intensity ratio between D and G peaks are included for both GO and HGO-4h.

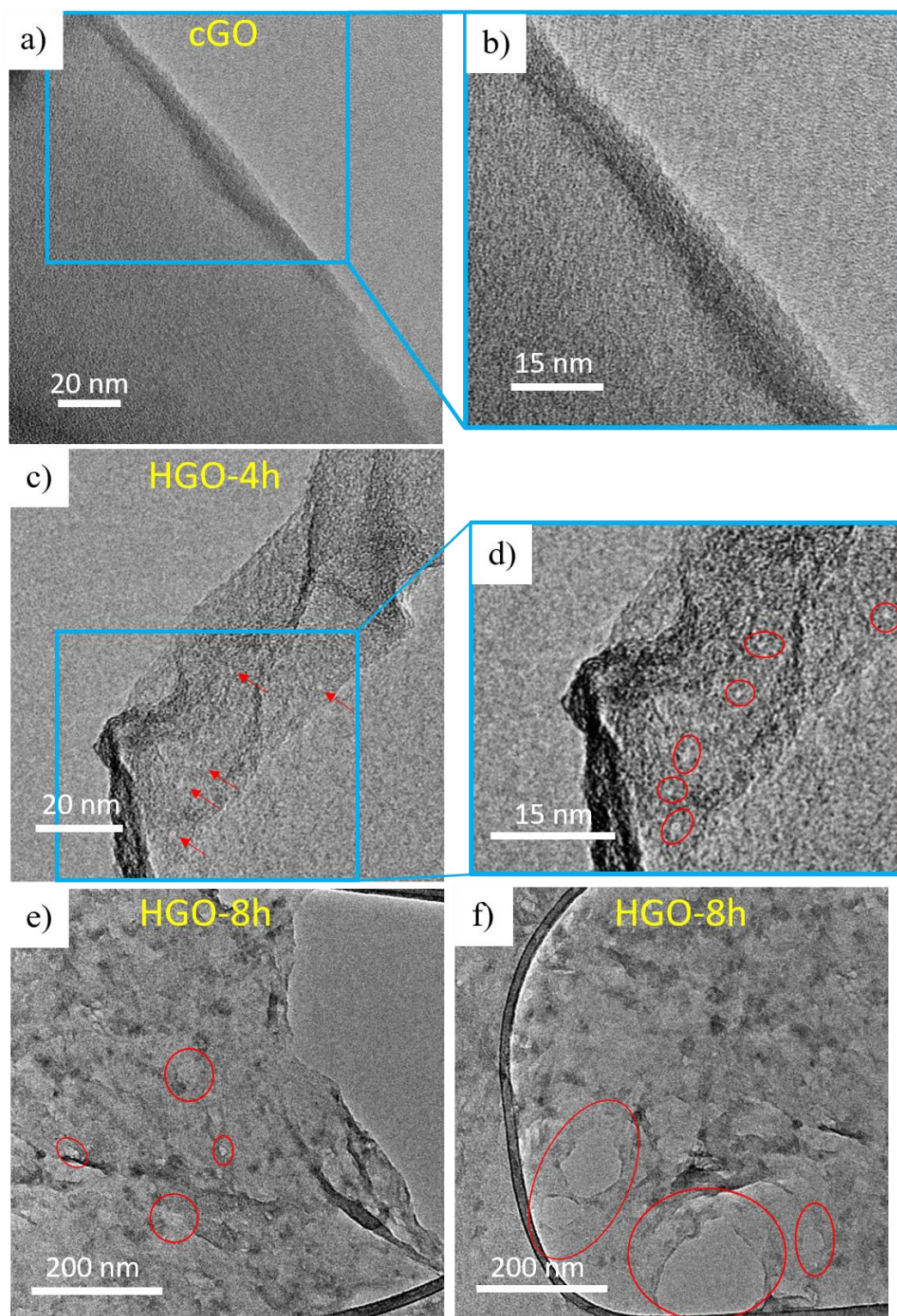## 2.5.   TEM imaging of GO, cGO, HGO-4h and HGO-8h

Figure S7. TEM images of cGO (a) and HGO-4h (c) at high magnification. The images on the right (b and d) correspond to the amplified area contained in the blue square on the left-hand side image. TEM images of HGO-8h (e and f) at low magnification.

10

2.6. Nuclear magnetic resonance (NMR)

Four NMR signals (labelled as **a**, **b**, **c** and **d**) arise from a different chemical environment for each proton. Aromatic protons (**c** and **d**) appear at higher frequency and therefore a larger chemical shift because of diamagnetic anisotropy effects experienced by protons in the aromatic ring. Aliphatic protons in sp^3 carbon atoms without neighboring electronegative elements, such as **a** and **b** protons, suffer small chemical shifts (at 1.3 and 2.3 ppm, respectively). The ratio of the area for the different peaks agrees with the stoichiometry of each proton in the polymer structure; 6:2:1:1 for a, b, c and d protons, respectively. The presence of very small peaks next to **c** and **d** protons at 6.3 and 6.7 ppm is associated with branched structures.[14] Apart from these PIM-1 characteristic bands, two signals corresponding to chloroform (at 7.3 ppm) and water (at 1.7 ppm) are also observed. The results presented here are in line with those ones found in the literature.[15-16]
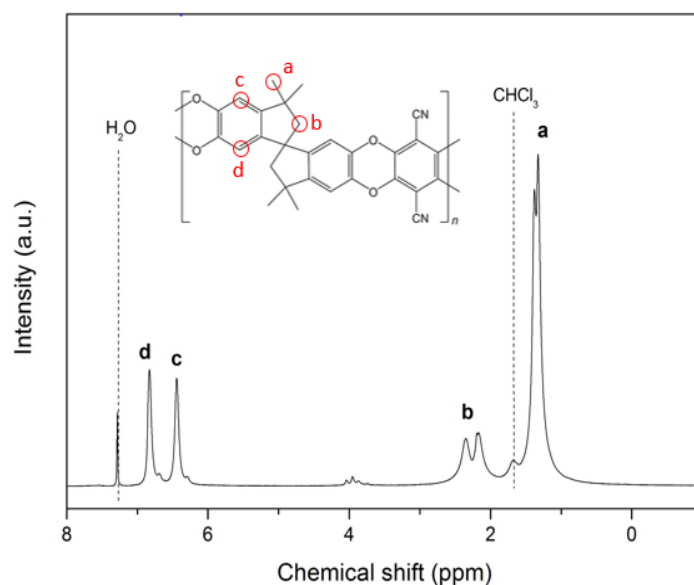

Figure S8. NMR spectra of PIM-1 together with the PIM-1 structure indicating the atoms that give rise to the four main peaks.

2.7. Elemental analysis of PIM-1, HGO-4h and P-H24

The content of C, H and N (as wt %) obtained by elemental analysis for PIM-1, HGO-4 and P-H24 is shown in Table S2. The content of O is not included in Table S2 since it could not be obtained due to limitations in the technique. However, O is expected to be present in PIM-1, HGO-4h and P-H24, and then the amount of O is calculated assuming that PIM-1, HGO-4h and P-H24 are only made of C, H, N and O. As can be seen in the table, HGO-4 shows no presence of N at all, whereas a considerable amount of N is found in PIM-1 and P-H24. Hence, it is hypothesized that the presence of N in P-H24 is related to the formation of PIM-1. Thus, based on the assumption that all N comes from PIM-1 polymer chains and using the theoretical weight ratio of PIM-1 (76.3 wt % C, 3.5 wt % H, 6.2 wt % N and 14 wt % O), the content of PIM-1 in P-H24 can be estimated.

Table S2. Elemental analysis of HGO-4h, PIM-1 and P-H24 showing the content of C, H and N in each sample as wt %. O content is estimated as explained above. Calculated PIM-1 content according to the procedure explained above is also included.

Sample	Wt % C	Wt % H	Wt % N	Wt % O (estimated)	Calculated PIM-1 wt %
HGO-4h	47.6	2.5	0	49.9	0
PIM-1	73.1	4.2	6.0	16.7	100
P-H24	68.1	3.8	5.3	22.8	88.4

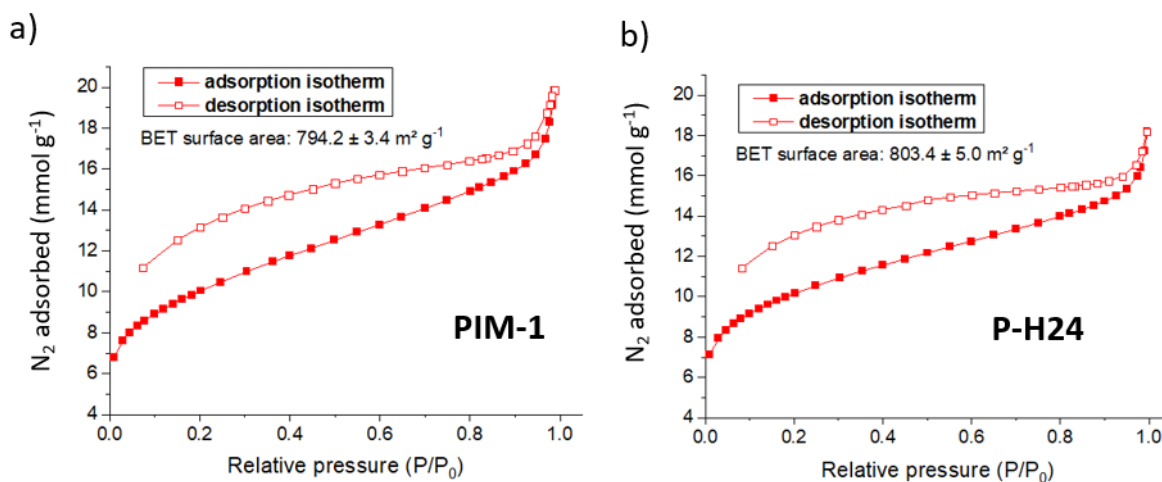## 2.8.   N2 sorption characterization of PIM-1 and P-H24

Figure S9. N2 adsorption and desorption isotherms of PIM-1 (a) and P-H24 (b) at 77 K.

2.9.   FT-IR characterization of PIM-1, HGO-4, P-H24 and f-P-H24
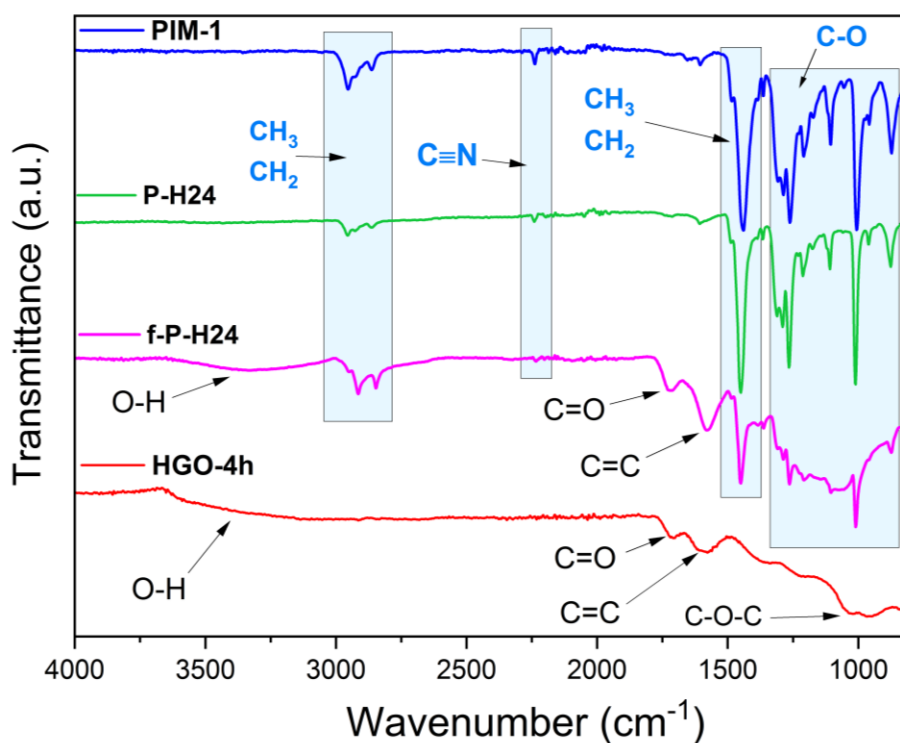

Figure S10. FT-IR spectra of PIM-1, P-H24, f-P-H24 and HGO-4h. The characteristic bands of PIM-1 are indicated by a blue inset for all the spectra containing PIM-1 moieties.

13

2.10. XPS characterization of PIM-1 and f-P-H24

Figure S11 shows the O1s high resolution spectra of PIM-1 and f-P-H24. As can be seen, the spectrum corresponding to f-P-H24 is a combination of both PIM-1 (i.e. C-O-C and C-OH[17-18]) and HGO-4h (i.e. COOH, C-O and C=O[19-20]). During the synthesis of P-H24, nucleophilic aromatic substitution reactions are believed to occur in the TFTPN monomers by the hydroxyl and epoxide (i.e. C-O) functional groups in HGO-4h. In order to evaluate the existence of this sort of chemical reaction, the ratio between the area of both peaks corresponding to HGO-4h (i.e. the C-O at 532.8 eV and the C=O peak at 531.5 eV) was calculated and compared for HGO-4h and f-P-H24. The higher C-O/C=O area ratio observed for HGO-4h (i.e. area ratio of 12.6, Figure S3c) as compared to f-P-H24 (i.e. area ratio of 2.8, Figure S11b) indicates lower amount of C-O groups (from HGO-4h) after the PIM-1 functionalization; i.e. hydroxyl and epoxide functional groups (C-O) have reacted with the TFTPN monomers leading to the formation of ether linkages characteristic from PIM-1 (C-O bond at 533.9 eV).

Figure S11. O1s high resolution XPS spectra of PIM-1 (a) and f-P-H24 (b). In all the XPS spectra, the green line represents the acquired XPS signal, whereas the black line corresponds to the fitted spectrum which includes the contributions of all the individual peaks.

14

Figure S12 displays the N1s high resolution spectra of PIM-1 and f-P-H24 where the presence of nitrile groups appears in both spectra as the only component. This indicates that the nitrile group from the TFTPN monomers remains chemically unaffected during the synthesis of P-H24. Chemical reactions between the nitrile group in TFTPN monomers and the functional groups in HGO-4h would result in multiple C-N peaks and then a shift in the position of the peak or/and a broader peak.[21-22]
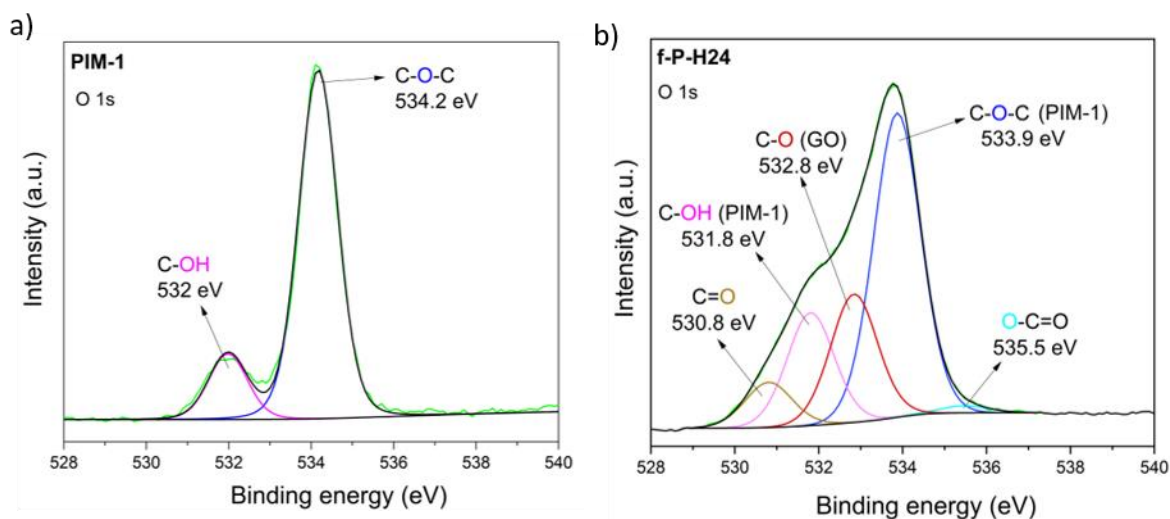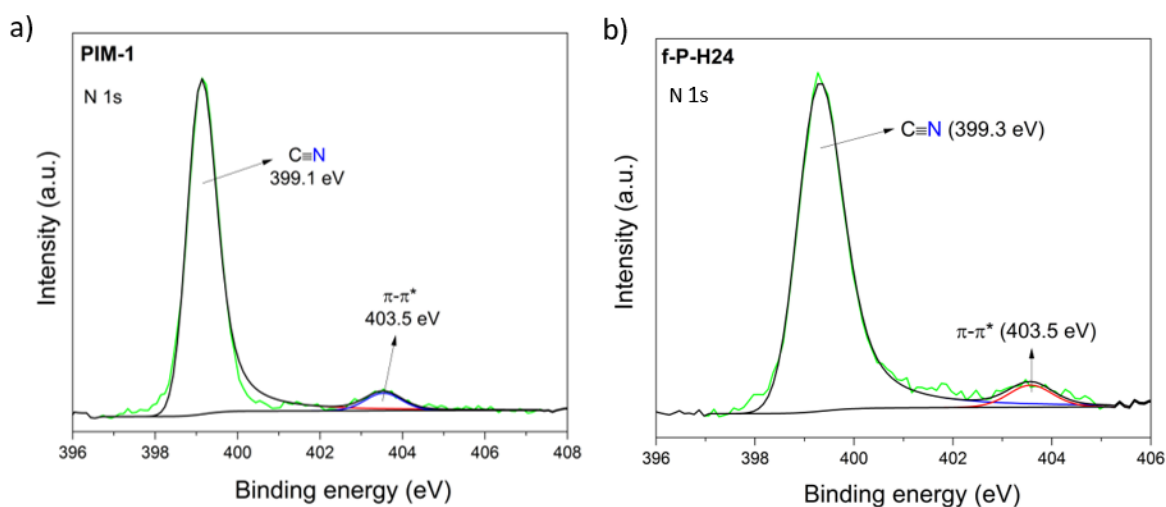

Figure S12. N1s high resolution XPS spectra of PIM-1 (a) and f-P-H24 (b). In all the XPS spectra, the green line represents the acquired XPS signal, whereas the black line corresponds to the fitted spectrum which includes the contributions of all the individual peaks.

Similar to the explanation above Table S2 (elemental analysis), the degree of PIM-1 functionalization of HGO-4h is calculated based on the assumption that all N present in f-P-H24 comes from the PIM-1 polymer chains attached to the graphene nanosheet.

Table S3. Atomic % of C, N and O for PIM-1 and f-P-H24 obtained by XPS measurements.

Sample	%C	%N	%O
PIM-1	84.8	4.4	10.8
f-P-H24	80.6	3.2	16.2

2.11. TGA characterization of PIM-1, HGO-4h, P-H24 and f-P-GO24

Figure S13 shows the TGA curves of PIM-1, P-H24, f-P-H24 and HGO-4h. The PIM-1 thermogravimetric curve exhibits a small weight loss (4.5%) between 35 and 150 °C associated with the removal of water, and a major weight loss of 41.8% after 450 °C that is related to the scission of ether linkages and consequently degradation of the polymeric chains.[21, 23-24] HGO-4h shows three well defined weight losses associated with the removal of adsorbed water (35-150 °C, weight loss of 18.1%), oxygen-containing functional groups (150-250 °C, weight loss of 23%) and pyrolysis of graphitic skeleton (400-800 °C, weight loss of 8.7%).[25-26] The thermogravimetric curve of P-H24 resembles that of PIM-1, which suggests that most of P-H24 corresponds to PIM-1 polymeric chains as expected. In turn, the thermogravimetric curve of f-P-H24 display features from both HGO-4h and PIM-1. Within the temperature range corresponding to removal of oxygen-containing functional groups (i.e. 150-250 °C), f-P-H24 shows a significantly higher weight loss of 5.5% as compared to PIM-1 (1.9%), but considerably lower than that seen in the thermogravimetric curve of HGO-4h (23%). This suggests that most of the functional groups present in HGO-4h have reacted with TFTPN monomers resulting in the formation of ether linkages and covalent attachment of PIM-1 to the graphene nanosheet. The weight loss observed in the thermogravimetric curve of f-P-H24 within 400 and 800 °C is then attributed mostly to the degradation of polymer chains attached.
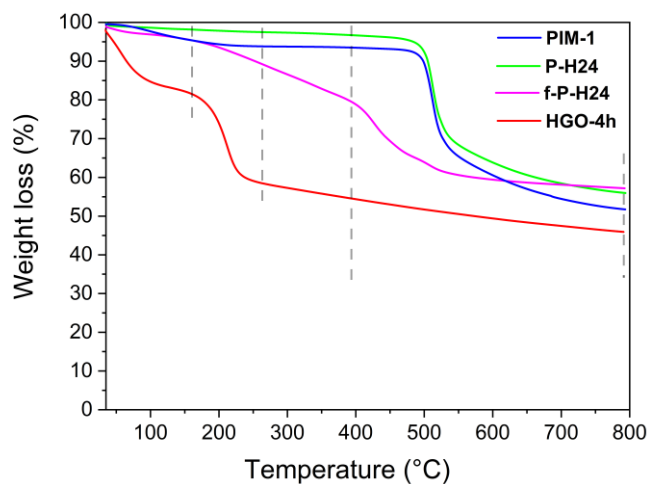
16

Figure S13. Thermogravimetric curves of PIM-1, P-H24, f-P-H24 and HGO-4h. Dash lines define the temperature windows in which decomposition of different functional groups takes place.

The weight losses occurring within each temperature range are presented in Table S4. In addition, the content of PIM-1 in P-H24 and f-P-H24 has been estimated using the corresponding weight losses between 400 and 800 °C, attributed to degradation of the PIM-1 polymer chains. As seen in Table S4 and Figure S13, a small contribution from the pyrolysis of graphitic structure is expected in the weight loss values of P-H24 and f-P-H24. Hence, the PIM-1 content in P-H24 and f-P-H24 can be calculated using the following equations, assuming that, within the studied temperature range, the maximum weight loss corresponds to PIM-1 (41.8%) and the minimum to HGO-4h (8.7%):

$$\text{PIM wt \% in P--H24} = \frac{WL_{P-H24}-WL_{HGO-4h}}{WL_{PIM}-WL_{GO}} \tag{1}$$

$$\text{PIM wt \% in f--P--H24} = \frac{WL_{f-P-H24}-WL_{HGO-4h}}{WL_{PIM}-WL_{HGO-4h}} \tag{2}$$

Where WL (%) corresponds to the weight losses between 400 and 800 ºC. Thus, WL_{PIM-1}, WL_{P-H24}, $WL_{f-P-H24}$ and WL_{HGO-4h} stand for the weight losses of PIM-1, P-H24, f-P-H24 and HGO-4h, respectively.

Table S4. Weight loss (%) in each step and PIM-1 content of all analyzed samples: PIM-1, HGO-4h, P-H24 and f-P-H24.

Sample	35-150 °C (%)	150-250 °C (%)	400-800 °C (%)	Calculated PIM-1 wt %
PIM-1	4.5	1.9	41.8	100
HGO-4h	18.1	23	8.7	0
P-H24	1.8	0.7	40.5	96
f-P-H24	4.2	5.5	21.9	40

2.12. UV-Vis characterization of PIM-1, HGO-4h, P-H24 and f-P-H24

Figure S14 displays the UV-Vis absorption spectra of PIM-1, f-P-H24 and HGO-4h. Pure PIM-1 shows two main peaks at 290 and 430 nm attributed to σ-π and π-π* transitions, respectively.[27] The spectrum of HGO-4h shows strong radiation scattering that increases as the wavelength becomes lower and a shoulder at 306 nm assigned to n-π* transitions taking place in the carbonyl groups.[28-29] The use of chloroform as solvent impedes the acquisition of the UV-Vis spectra at wavelengths below 240 nm, which hinders the observation of the main peak of HGO-4h at 230 nm arising from π-π* transitions. The spectrum corresponding to f-P-H24 shows both transitions attributed to PIM-1 and scattering effects associated to the graphene structure.
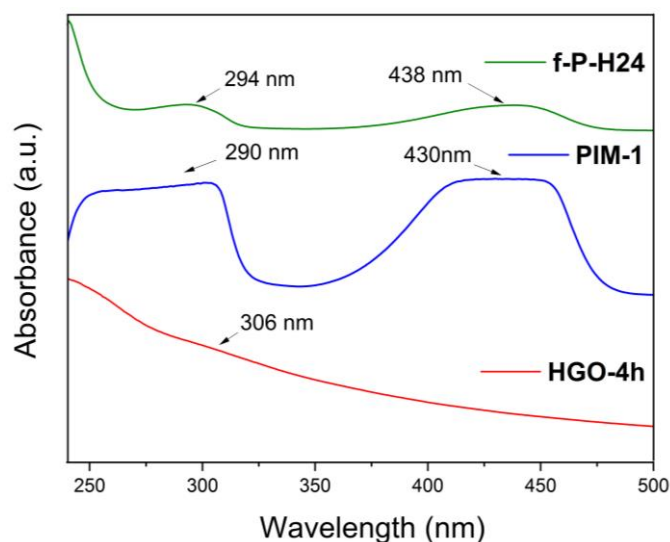
Figure S14. UV-Vis absorption spectra of: HGO-4h, PIM-1 and f-P-H24. All the solutions were prepared in chloroform with a concentration of 0.5 mg ml^{-1}. Note that at this concentration, the spectrum of PIM-1 looks slightly saturated.

Figure S15a and 15b show the UV-Vis absorbance curves of PIM-1 used for the calibration and the linear fit obtained, respectively. Figure S15c displays the average UV-Vis absorbance curves of P-H24 and f-P-H24 within 350 and 700 nm. As can be observed, P-H24 shows minimal scattering since it is mostly made of pure PIM-1 (~90 wt % as suggested by elemental analysis and TGA). The average absorbance values at 430 nm for P-H24 and f-P-H24 were obtained by subtracting the background to eliminate the effect of the scattering, and then were interpolated in the equation shown in Figure S15b to calculate the content of PIM-1 in P-H24 and f-P-H24.
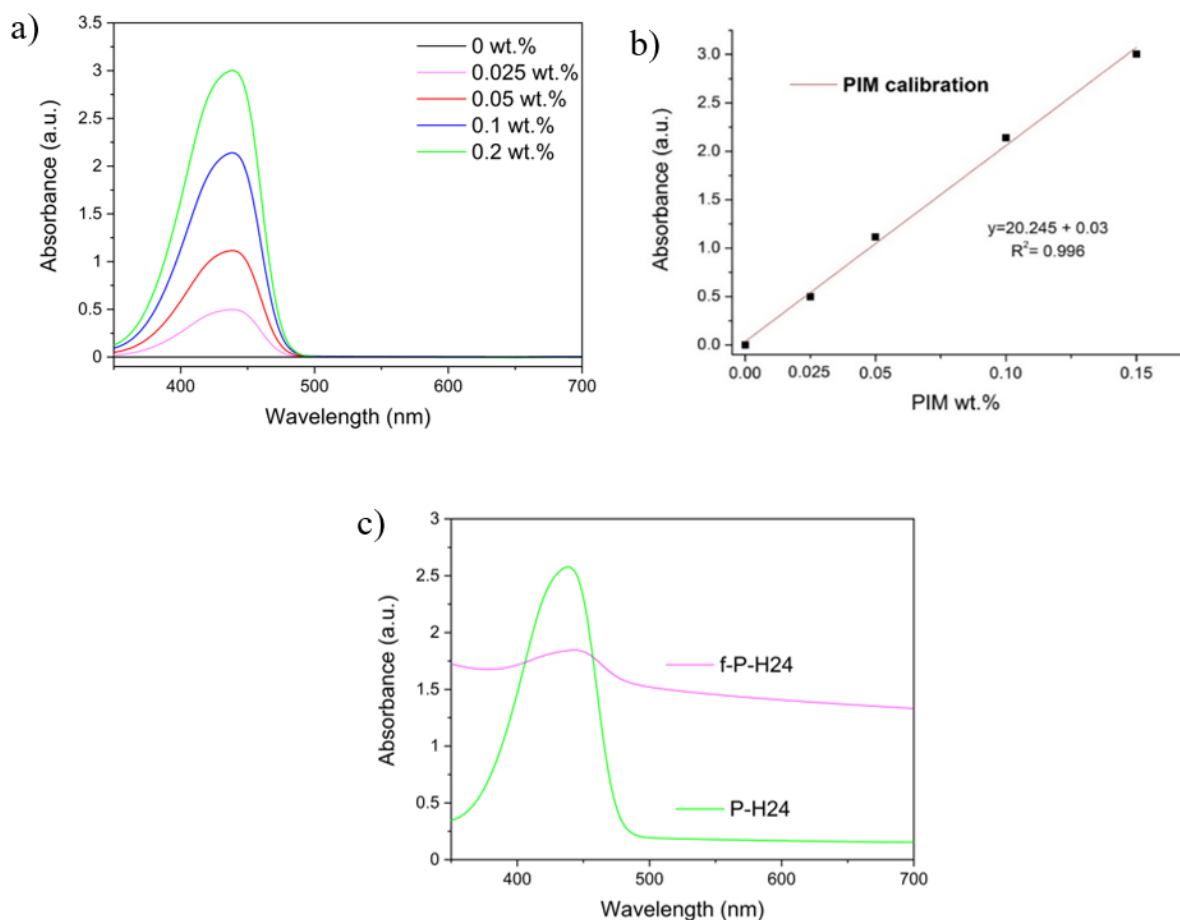
Figure S15. UV-Vis absorbance curves at different concentrations of PIM-1 in chloroform (a), PIM-1 linear fit at 430 nm (b) and average UV-Vis absorbance curves of P-H24 and f-P-H24 used in the calculations of the PIM-1 content (c). In both P-H24 and f-P-H24 spectra (c), the contribution of the scattering was minimized by subtracting the background. A concentration of 0.125 and 0.33 mg ml^{-1} was used to prepare P-H24 and f-P-H24 dispersions in chloroform, respectively.

2.13. TEM characterization of PIM-1 and f-P-H24
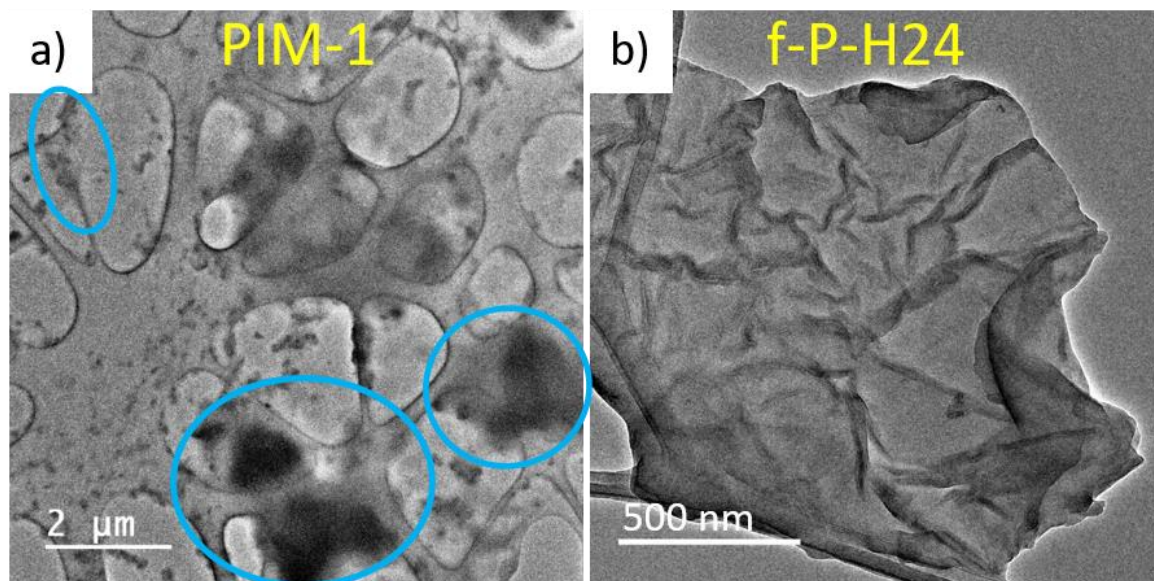
Figure S16. TEM image of PIM-1 (a) and f-P-H24 (b). Blue circles on the left-hand side image indicates the presence of PIM-1 on the surface of the lacey carbon TEM grid.

2.14. SEM characterization of PIM-1 and MMMs containing ODA-HGO-4h and P-H24 nanofillers
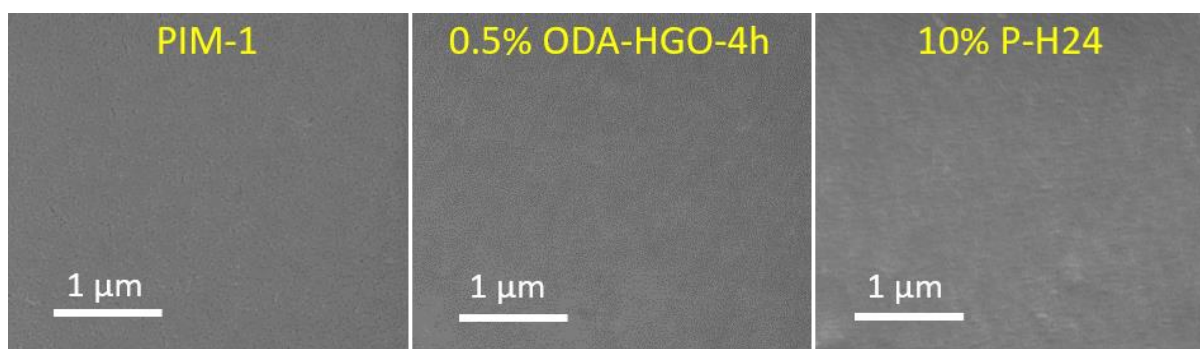
Figure S17. Top-view SEM images of PIM-1 membranes (a) and MMMs: 10% P-H24 (b) and 0.5% ODA-HGO-4h (c).

2.15. Micrometer measurements of PIM-1 and MMMs containing ODA-HGO-4h and P-H24 nanofillers

Table S5. Average and standard deviation membrane thickness measurements calculated using a digital micrometer screw gauge.

Membrane	Thickness (μm)	Membrane	Thickness (μm)
PIM-1	52 ± 7	-	-
1% P-H24	50 ± 4	0.1% ODA-HGO-4h	48 ± 3
5% P-H24	48 ± 3	0.2% ODA-HGO-4h	53 ± 4
10% P-H24	47 ± 4	0.5% ODA-HGO-4h	52 ± 3

2.16. CO$_2$/CH$_4$ separation performance of MMMs containing ODA-HGO-4h and P-H24 nanofillers
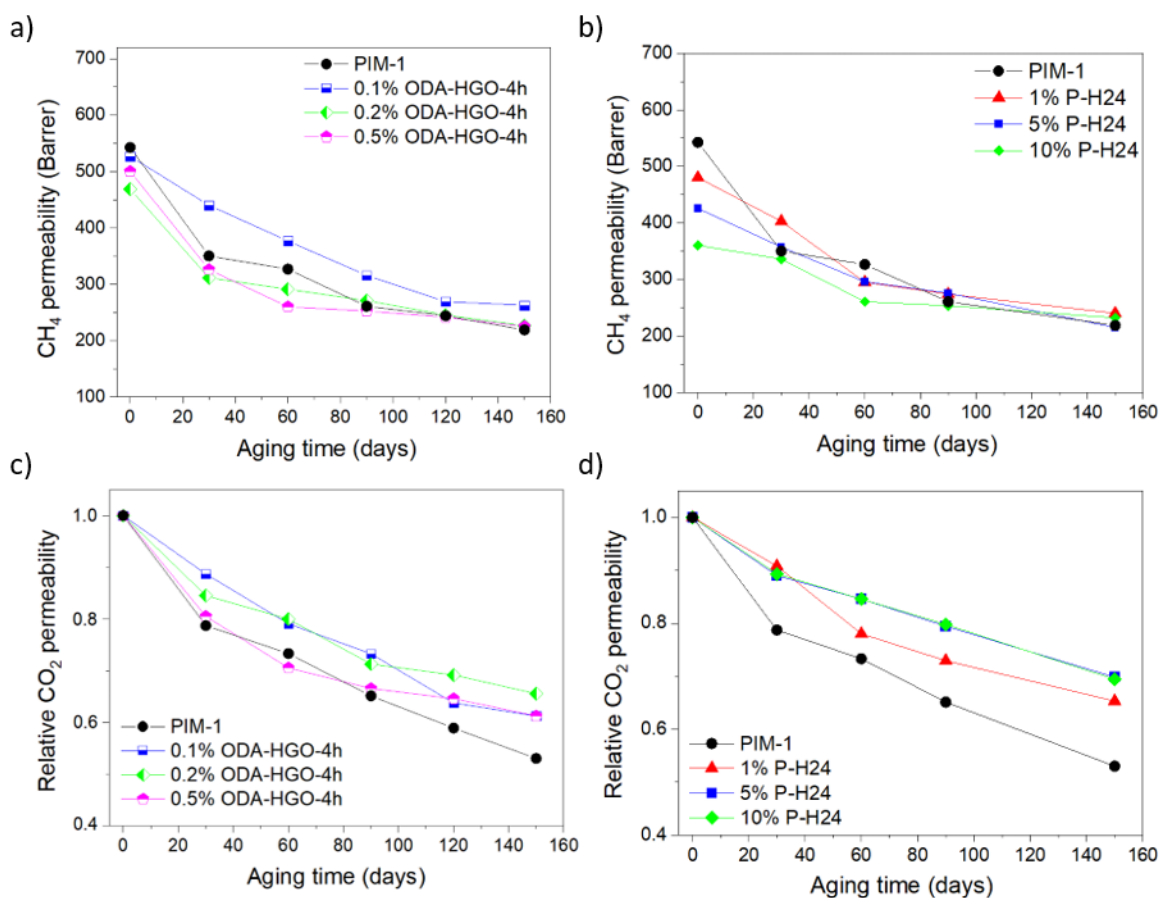
Figure S18. CH$_4$ permeabilities (a) and relative to initial CO$_2$ permeabilities (c) of PIM-1 and MMMs containing ODA-HGO-4h. CH$_4$ permeabilities (b) and relative to initial CO$_2$ permeabilities (d) of PIM-1 and MMMs containing P-H24.

2.17. Average and standard deviation data corresponding to CO_2 and CH_4 permeability, CO_2/CH_4 selectivity, CO_2 permeability drop and relative CO_2 permeability of PIM-1 and MMMs containing ODA-HGO-4h and P-H24 nanofillers.

Table S6. Average CO_2 permeability values of PIM-1 and MMMs using ODA-HGO-4h and P-H24 as nanofiller with their corresponding standard deviation.

Aging time (Days)	CO₂ permeability (Barrer)						
	PIM-1	0.1% ODA-HGO-4h	0.2% ODA-HGO-4h	0.5% ODA-HGO-4h	1% P-H24	5% P-H24	10% P-H24
0	6,190 ± 812	6,146 ± 831	5,429 ± 649	5,525 ± 616	5,675 ± 427	5,223 ± 382	4,727 ± 449
30	4,874 ± 829	5,452 ± 537	4,590 ± 477	4,448 ± 311	5,153 ± 388	4,649 ± 63	4,222 ± 142
60	4,538 ± 837	4,859 ± 441	4,341 ± 729	3,898 ± 269	4,428 ± 335	4,420 ± 58	3,999 ± 264
90	4,032 ± 858	4,503 ± 548	3,918 ± 600	3,677 ± 433	4,140 ± 365	4,150 ± 343	3,772 ± 404
120	3,647 ± 705	3,898 ± 377	3,755 ± 816	3,569 ± 339	-	-	-
150	3,283 ± 870	3,763 ± 354	3,559 ± 815	3,383 ± 350	3,707 ± 432	3,648 ± 438	3,283 ± 321

Table S7. Average CH_4 permeability values of PIM-1 and MMMs using ODA-HGO-4h and P-H24 as nanofiller with their corresponding standard deviation.

Aging time (Days)	CH$_4$ permeability (Barrer)						
	PIM-1	0.1% ODA-HGO-4h	0.2% ODA-HGO-4h	0.5% ODA-HGO-4h	1% P-H24	5% P-H24	10% P-H24
0	543 ± 104	527 ± 105	469 ± 89	500 ± 96	480 ± 102	426 ± 107	360 ± 91
30	350 ± 92	440 ± 64	311 ± 78	326 ± 29	403 ± 42	357 ± 17	336 ± 51
60	327 ± 87	377 ± 52	291 ± 68	260 ± 34	295 ± 42	296 ± 40	261 ± 51
90	261 ± 81	316 ± 44	271 ± 56	252 ± 44	274 ± 33	276 ± 39	254 ± 41
120	244 ± 69	269 ± 24	245 ± 39	241 ± 18	-	-	-
150	219 ± 73	263 ± 31	226 ± 46	225 ± 19	240 ± 51	215 ± 38	232 ± 120

Table S8. Average CO_2/CH_4 selectivities of PIM-1 and MMMs using ODA-HGO-4h and P-H24 as nanofiller with their corresponding standard deviation.

Aging time (Days)	CO₂/CH₄ selectivity						
	PIM-1	0.1% ODA-HGO-4h	0.2% ODA-HGO-4h	0.5% ODA-HGO-4h	1% P-H24	5% P-H24	10% P-H24
0	11.7 ± 1.8	11.8 ± 1.0	11.8 ± 2.2	11.3 ± 1.3	12.2 ± 1.9	12.9 ± 2.7	13.6 ± 2.3
30	14.4 ± 2.2	12.7 ± 0.8	14.7 ± 2.8	13.7 ± 1.0	12.8 ± 0.7	13.0 ± 0.7	12.8 ± 1.9
60	14.3 ± 2.0	14.2 ± 1.2	15.1 ± 1.6	15.2 ± 1.8	15.2 ± 2.0	15.2 ± 2.0	15.7 ± 2.2
90	16.2 ± 3.0	14.3 ± 0.9	14.5 ± 1.4	14.8 ± 1.2	15.2 ± 1.0	15.3 ± 2.2	15.0 ± 1.2
120	15.6 ± 2.7	14.5 ± 0.8	15.2 ± 2.0	14.8 ± 0.9	-	-	-
150	15.6 ± 2.6	14.4 ± 1.7	15.7 ± 1.2	15.1 ± 0.9	15.8 ± 1.8	17.2 ± 1.4	16.1 ± 4.0

Table S9. CO_2 permeability drops of PIM-1 and MMMs using ODA-HGO-4h and P-H24 as nanofiller.

Aging time (Days)	CO₂ permeability drop (Barrer)						
	PIM-1	0.1% ODA-HGO-4h	0.2% ODA-HGO-4h	0.5% ODA-HGO-4h	1% P-H24	5% P-H24	10% P-H24
0	0	0	0	0	0	0	0
30	1,317	694	839	1,076	522	575	505
60	1,652	1,286	1,087	1,627	1,246	804	728
90	2,159	1,643	1,558	1,847	1,535	1,074	955
120	2,543	2,228	1,673	1,956	-	-	-
150	2,908	2,383	1,870	2,141	1,968	1,576	1,445

Table S10. Relative to initial CO_2 permeabilities of PIM-1 and MMMs using ODA-HGO-4h and P-H24 as nanofiller.

Aging time (Days)	Relative CO₂ permeability						
	PIM-1	0.1% ODA-HGO-4h	0.2% ODA-HGO-4h	0.5% ODA-HGO-4h	1% P-H24	5% P-H24	10% P-H24
0	1	1	1	1	1	1	1
30	0.79	0.89	0.85	0.81	0.91	0.89	0.89
60	0.73	0.79	0.80	0.71	0.78	0.85	0.85
90	0.65	0.73	0.71	0.67	0.73	0.79	0.80
120	0.59	0.64	0.69	0.65	-	-	-
150	0.53	0.61	0.66	0.61	0.65	0.70	0.70

2.18. Rationalization of the MMMs gas separation performance using the Maxwell model

The Maxwell-Wagner-Sillars equation (Eq. S3) was used to investigate the permeability of both nanofillers, ODA-HGO and P-H24.

$$P_M = P_p \frac{nP_f + (1-n)\,P_p + (1-n)(P_f - P_p)\emptyset}{nP_f + (1-n)\,P_p - n\,(P_f - P_p)\emptyset} \tag{S3}$$

where P_M, P_p and P_f account for the gas permeabilities of the MMM, polymer phase and filler, respectively, $\emptyset$ represents the volume ratio and n is the shape factor related to the geometry and the orientation of the filler.

The calculation of the volume ratio ($\emptyset$) was carried out using the wt.% of each MMM, the density of graphene oxide was obtained as the two-dimensional mass density of a graphene single layer (7.63 x 10^{-8} g cm^{-2}) divided by the thickness of a GO flake (1 nm),[30-31] and the density of PIM-1 was assumed 0.948 g cm^{-3} as reported elsewhere.[32]

ODA-HGO nanofillers

First, the *n* parameter was calculated for each MMM containing non-porous ODA-GO by substituting P_M (experimental permeability of MMM[33]), P_p (experimental permeability of pure PIM-1[33]) and P_f (equals 0) in Eq. S3, and the obtained values are shown in Table S11.

Table S11. Values of the *n* parameter for CO_2 and CH_4 of each MMM containing ODA-GO nanofillers.

MMM	*n* factor (from CO_2)	*n* factor (from CH_4)
0.1% ODA-GO	0.996	0.996
0.25% ODA-GO	0.993	0.990

Later, the n values shown in Table S11 were included in Eq. S3 along with the experimental CO_2 (Table S6) and CH_4 (Table S7) permeability values of membranes containing 0.1%, 0.2% and 0.5% ODA-HGO membranes, and P_f for the porous fillers were calculated (Table S12). The n value of 0.1% ODA-HGO was assumed to be the same as those for 0.1% ODA-GO since both nanofillers are expected to have very similar shape and orientation (the only difference is the presence of holes). However, for 0.2% and 0.5% ODA-HGO, the n values of these membranes were assumed to be that of 0.25% ODA-GO, which was the closest loading available in the work by Alberto et al.[33] As seen in Table S12, P_f can be calculated for all MMMs.

Table S12. CO_2 and CH_4 permeabilities of MMMs containing P-H24 nanofillers.

MMM	CO_2 permeability (Barrer)	CH_4 permeability (Barrer)
0.1% ODA-HGO	898	19.4
0.2% ODA-HGO	63	3.3
0.5% ODA-HGO	262	31.9

P-H24 nanofillers

Following a similar strategy to that explained above, the n parameter for MMMs containing 1%, 5% and 10% P-GO24 were calculated and are shown in Table S13. It is important to notice that n values at comparable loadings are similar for both gases.

Table S13. Values of the n parameter for CO_2 and CH_4 of each MMMs containing P-GO24 nanofillers.

MMMs	n factor (from CO_2)	n factor (from CH_4)
1% P-GO24	0.991	0.995
5% P-GO24	0.965	0.983
10% P-GO24	0.956	0.956

Later, P_f was calculated using the experimental CO_2 and CH_4 permeabilities of P-H24. However, these values were negative or just above 0. This is due to the very similar permeabilities of MMMs containing P-GO24[34] and P-H24 (Table S6 and Table S7), as explained in the main manuscript. Nevertheless, P-GO24 and P-H24 MMMs exhibit remarkably different CO_2 and CH_4 permeabilities after 150 days of physical aging and thus, P_f can be calculated using the permeability values of the aged MMMs.

When physical aging takes place, the gas permeabilities of the polymer phase is affected by the presence of the nanofiller, this means that the permeability of PIM-1 in the MMMs must be higher than in the pure PIM-1 membrane. Using Eq. S3 and assuming that P_M corresponds to the permeability of MMMs obtained experimentally[34] and P_f equals 0, P_p was calculated (Table S14). These values correspond to the gas permeabilities of the polymer phase in each MMMs after 150 days. As expected, the membrane with the higher loading has the polymer phase with the highest CO_2 and CH_4 permeabilities.

Table S14. Values of CO_2 and CH_4 permeabilities of the polymer phase (P_p) in MMMs containing P-GO24 nanofillers.

MMM	CO₂ permeability (Barrer)	CH₄ permeability (Barrer)
1% P-GO24	3563	232
5% P-GO24	3804	272
10% P-GO24	4010	253

Using the calculated P_p (Table S14) and n values (Table S13), along with the experimental gas permeabilities for P-H24 (P_M) and the corresponding $\emptyset$, P_f was calculated for each MMM and shown in Table S15. As can be observed, 5% and 10% P-H24 provides a reasonable P_f value, whereas 1% P-H24 exhibits a negative value. This anomalous negative value is due to P_M (Table S6 and Table S7) being higher than P_P (Table S14). In these circumstances, the Maxwell-Wagner-Sillars equation often returns a negative P_f value which mathematically solves the equation but does not correspond to the real permeability value.

Table S15. Values of CO_2 and CH_4 permeabilities (P_f) of P-H24 nanofillers.

MMM	CO₂ permeability (Barrer)	CH₄ permeability (Barrer)
1% P-H24	(-151)	(-10.7)
5% P-H24	379	1.7
10% P-H24	51	21.1

References

(1) Xu, Y. X.; Chen, C. Y.; Zhao, Z. P.; Lin, Z. Y.; Lee, C.; Xu, X.; Wang, C.; Huang, Y.; Shakir, M. I.; Duan, X. F. Solution Processable Holey Graphene Oxide and Its Derived Macrostructures for High-Performance Supercapacitors. *Nano Letters* **2015,** *15* (7), 4605-4610, DOI: 10.1021/acs.nanolett.5b01212.

(2) Konios, D.; Stylianakis, M. M.; Stratakis, E.; Kymakis, E. Dispersion Behaviour of Graphene Oxide and Reduced Graphene Oxide. *J. Colloid Interface Sci.* **2014,** *430*, 108-112, DOI: 10.1016/j.jcis.2014.05.033.

(3) Xu, Y. X.; Lin, Z. Y.; Zhong, X.; Huang, X. Q.; Weiss, N. O.; Huang, Y.; Duan, X. F. Holey Graphene Frameworks for Highly Efficient Capacitive Energy Storage. *Nature Communications* **2014,** *5*, DOI: 10.1038/ncomms5554.

(4) Huang, L. Y.; Lu, C. X.; Wang, F.; Dong, X. Z. Piezoelectric Property of PVDF/Graphene Composite Films Using 1h, 1h, 2h, 2h-Perfluorooctyltriethoxysilane as a Modifying Agent. *Journal of Alloys and Compounds* **2016,** *688*, 885-892, DOI: 10.1016/j.jallcom.2016.07.058.

(5) Jang, J.; Viet Hung, P.; Hur, S. H.; Chung, J. S. Dispersibility of Reduced Alkylamine-Functionalized Graphene Oxides in Organic Solvents. *J. Colloid Interface Sci.* **2014,** *424*, 62-66, DOI: 10.1016/j.jcis.2014.03.018.

(6) Bandyopadhyay, P.; Park, W. B.; Layek, R. K.; Uddin, M. E.; Kim, N. H.; Kim, H.-G.; Lee, J. H. Hexylamine Functionalized Reduced Graphene Oxide/Polyurethane Nanocomposite-Coated Nylon for Enhanced Hydrogen Gas Barrier Film. *J. Membr. Sci.* **2016,** *500*, 106-114, DOI: 10.1016/j.memsci.2015.11.029.

(7) Huang, S. Q.; Dakhchoune, M.; Luo, W.; Oveisi, E.; He, G. W.; Rezaei, M.; Zhao, J.; Alexander, D. T. L.; Zuttel, A.; Strano, M. S.; Agrawal, K. V. Single-Layer Graphene Membranes by Crack-Free Transfer for Gas Mixture Separation. *Nature Communications* **2018,** *9*, DOI: 10.1038/s41467-018-04904-3.

(8) Carlsson, J. M.; Hanke, F.; Linic, S.; Scheffler, M. Two-Step Mechanism for Low-Temperature Oxidation of Vacancies in Graphene. *Physical Review Letters* **2009,** *102* (16), DOI: 10.1103/PhysRevLett.102.166104.

(9) Yang, X.; Mei, T.; Yang, J.; Zhang, C.; Lv, M.; Wang, X. Synthesis and Characterization of Alkylamine-Functionalized Graphene for Polyolefin-Based Nanocomposites. *Applied Surface Science* **2014,** *305*, 725-731, DOI: 10.1016/j.apsusc.2014.03.184.

(10) Bai, Y. L.; Yang, X. F.; He, Y. B.; Zhang, J. Y.; Kang, L. P.; Xu, H.; Shi, F.; Lei, Z. B.; Liu, Z. H. Formation Process of Holey Graphene and Its Assembled Binder-Free Film Electrode with High Volumetric Capacitance. *Electrochimica Acta* **2016,** *187*, 543-551, DOI: 10.1016/j.electacta.2015.11.090.

(11) Eckmann, A.; Felten, A.; Mishchenko, A.; Britnell, L.; Krupke, R.; Novoselov, K. S.; Casiraghi, C. Probing the Nature of Defects in Graphene by Raman Spectroscopy. *Nano Letters* **2012,** *12* (8), 3925-3930, DOI: 10.1021/nl300901a.

(12) Kudin, K. N.; Ozbas, B.; Schniepp, H. C.; Prud'homme, R. K.; Aksay, I. A.; Car, R. Raman Spectra of Graphite Oxide and Functionalized Graphene Sheets. *Nano Letters* **2008,** *8* (1), 36-41, DOI: 10.1021/nl071822y.

(13) Dimiev, A. M.; Tour, J. M. Mechanism of Graphene Oxide Formation. *Acs Nano* **2014,** *8* (3), 3060-3068, DOI: 10.1021/nn500606a.

(14) Foster, A. B.; Tamaddondar, M.; Luque-Alled, J. M.; Harrison, W. J.; Li, Z.; Gorgojo, P.; Budd, P. M. Understanding the Topology of the Polymer of Intrinsic Microporosity PIM-1: Cyclics, Tadpoles, and Network Structures and Their Impact on Membrane Performance. *Macromolecules* **2020,** *53* (231), 569-583, DOI: 10.1021/acs.macromol.9b02185.

(15) Satilmis, B.; Budd, P. M. Base-Catalysed Hydrolysis of PIM-1: Amide Versus Carboxylate Formation. *RSC Adv.* **2014,** *4* (94), 52189-52198, DOI: 10.1039/c4ra09907a.

(16) Tamaddondar, M.; Foster, A. B.; Luque-Alled, J. M.; Msayib, K. J.; Carta, M.; Sorribas, S.; Gorgojo, P.; McKeown, N. B.; Budd, P. M. Intrinsically Microporous Polymer Nanosheets for High-Performance Gas Separation Membranes. *Macromolecular Rapid Communications* **2020,** *41* (2), 8, DOI: 10.1002/marc.201900572.

(17) Song, Q. L.; Cao, S.; Pritchard, R. H.; Qiblawey, H.; Terentjev, E. M.; Cheetham, A. K.; Sivaniah, E. Nanofiller-Tuned Microporous Polymer Molecular Sieves for Energy and Environmental Processes. *J. Mater. Chem. A* **2016,** *4* (1), 270-279, DOI: 10.1039/c5ta09060a.

(18) Bonso, J. S.; Kalaw, G. D.; Ferraris, J. P. High Surface Area Carbon Nanofibers Derived from Electrospun PIM-1 for Energy Storage Applications. *Journal of Materials Chemistry A* **2014,** *2* (2), 418-424, DOI: 10.1039/c3ta13779a.

(19) Ossonon, B. D.; Belanger, D. Synthesis and Characterization of Sulfophenyl-Functionalized Reduced Graphene Oxide Sheets. *Rsc Advances* **2017,** *7* (44), 27224-27234, DOI: 10.1039/c6ra28311j.

(20) Muralikrishna, S.; Sureshkumar, K.; Varley, T. S.; Nagaraju, D. H.; Ramakrishnappa, T. In Situ Reduction and Functionalization of Graphene Oxide with L-Cysteine for Simultaneous Electrochemical Determination of Cadmium(Ii), Lead(Ii), Copper(Ii), and Mercury(Ii) Ions. *Analytical Methods* **2014,** *6* (21), 8698-8705, DOI: 10.1039/c4ay01945h.

(21) Li, F. Y.; Xiao, Y.; Chung, T.-S.; Kawi, S. High-Performance Thermally Self-Cross-Linked Polymer of Intrinsic Microporosity (PIM-1) Membranes for Energy Development. *Macromolecules* **2012,** *45* (3), 1427-1437, DOI: 10.1021/ma202667y.

(22) Han, W.; Zhang, C.; Zhao, M.; Yang, F.; Yang, Y.; Weng, Y. Post-Modification of PIM-1 and Simultaneously in Situ Synthesis of Porous Polymer Networks into PIM-1 Matrix to Enhance CO2 Separation Performance. *J. Membr. Sci.* **2021,** *636*.

(23) Du, N. Y.; Robertson, G. P.; Dal-Cin, M. M.; Scoles, L.; Guiver, M. D. Polymers of Intrinsic Microporosity (PIMs) Substituted with Methyl Tetrazole. *Polymer* **2012,** *53* (20), 4367-4372, DOI: 10.1016/j.polymer.2012.07.055.

(24) Song, Q. L.; Cao, S.; Pritchard, R. H.; Ghalei, B.; Al-Muhtaseb, S. A.; Terentjev, E. M.; Cheetham, A. K.; Sivaniah, E. Controlled Thermal Oxidative Crosslinking of Polymers of Intrinsic Microporosity Towards Tunable Molecular Sieve Membranes. *Nature Communications* **2014,** *5*, DOI: 10.1038/ncomms5813.

(25) Dang, T. T.; Pham, V. H.; Hur, S. H.; Kim, E. J.; Kong, B. S.; Chung, J. S. Superior Dispersion of Highly Reduced Graphene Oxide in N,N-Dimethylformamide. *J. Colloid Interface Sci.* **2012,** *376*, 91-96, DOI: 10.1016/j.jcis.2012.03.026.

(26) Fernandez-Merino, M. J.; Guardia, L.; Paredes, J. I.; Villar-Rodil, S.; Solis-Fernandez, P.; Martinez-Alonso, A.; Tascon, J. M. D. Vitamin C Is an Ideal Substitute for Hydrazine in the Reduction of Graphene Oxide Suspensions. *Journal of Physical Chemistry C* **2010,** *114* (14), 6426-6432, DOI: 10.1021/jp100603h.

(27) Rong, Y.; Large, M. J.; Tripathi, M.; Ogilvie, S. P.; Amorim Graf, A.; Mao, B.; Tunesi, J.; Salvage, J. P.; King, A. A. K.; Pasquazi, A.; Peccianti, M.; Malpass-Evans, R.; McKeown, N. B.; Marken, F.; Dalton, A. B. Charge Transfer Hybrids of Graphene Oxide and the Intrinsically Microporous Polymer PIM-1. *ACS Appl. Mater. Interfaces* **2019,** *11* (34), 31191-31199, DOI: 10.1021/acsami.9b09832.

(28) Zhang, J. L.; Yang, H. J.; Shen, G. X.; Cheng, P.; Zhang, J. Y.; Guo, S. W. Reduction of Graphene Oxide Via L-Ascorbic Acid. *Chem. Commun.* **2010,** *46* (7), 1112-1114, DOI: 10.1039/b917705a.

(29) Gupta, B. K.; Kedawat, G.; Kumar, P.; Rafiee, M. A.; Tyagi, P.; Srivastava, R.; Ajayan, P. M. An N-Type, New Emerging Luminescent Polybenzodioxane Polymer for Application in Solution-Processed Green Emitting Oleds. *Journal of Materials Chemistry C* **2015,** *3* (11), 2568-2574, DOI: 10.1039/c4tc02581d.

(30) Thomas, S.; Ajith, K. M.; Lee, S. U.; Valsakumar, M. C. Assessment of the Mechanical Properties of Monolayer Graphene Using the Energy and Strain-Fluctuation Methods. *RSC Adv.* **2018,** *8* (48), 27283-27292, DOI: 10.1039/c8ra02967a.

(31) Karssemeijer, L. J.; Fasolino, A. Phonons of Graphene and Graphitic Materials Derived from the Empirical Potential Lcbopii. *Surf. Sci.* **2011,** *605* (17-18), 1611-1615, DOI: 10.1016/j.susc.2010.10.036.

(32) Gonciaruk, A.; Althumayri, K.; Harrison, W. J.; Budd, P. M.; Siperstein, F. R. PIM-1/Graphene Composite: A Combined Experimental and Molecular Simulation Study. *Microporous Mesoporous Mat.* **2015,** *209*, 126-134, DOI: 10.1016/j.micromeso.2014.07.007.

(33) Alberto, M.; Bhavsar, R.; Luque-Alled, J. M.; Vijayaraghavan, A.; Budd, P. M.; Gorgojo, P. Impeded Physical Aging in PIM-1 Membranes Containing Graphene-Like Fillers. *J. Membr. Sci.* **2018,** *563*, 513-520, DOI: 10.1016/j.memsci.2018.06.026.

(34) Luque-Alled, J. M.; Ameen, A.; Alberto, M.; Tamaddondar, M.; Foster, A. B.; Budd, P. M.; Vijayaraghavan, A.; Gorgojo, P. Gas Separation Performance of MMMs Containing (PIM-1)-Functionalized Go Derivatives. *J. Membr. Sci.* **2020**.